




Aerosol Activation in Radiation Fog at the Atmospheric Radiation Program Southern Great Plains Site

 Charlotte Wainwright¹ , Rachel Y.-W. Chang² , and David Richter¹ 
¹Department of Civil and Environmental Engineering and Earth Sciences, University of Notre Dame, Notre Dame, IN, USA, ²Department of Physics and Atmospheric Science, Dalhousie University, Halifax, NS, Canada

Key Points:

- Supersaturation during eight radiation fog cases at a rural site in Oklahoma, USA is found to vary from 0.01% to 0.06%
- Evidence of initial dry particle size distribution and aerosol hygroscopicity affects nucleation scavenging efficiency
- The lowest dry activation diameter during each fog event was typically between 300–400 nm and wet activation diameters ranged from 2 to 7 μm

Correspondence to:

 C. Wainwright,
cwainwri@nd.edu

Citation:

 Wainwright, C., Chang, R. Y.-W., & Richter, D. (2021). Aerosol activation in radiation fog at the atmospheric radiation program Southern Great Plains site. *Journal of Geophysical Research: Atmospheres*, 126, e2021JD035358. <https://doi.org/10.1029/2021JD035358>

 Received 3 JUN 2021
 Accepted 25 OCT 2021

Abstract Environmental supersaturation is a key parameter in the formation of fog and clouds, yet it cannot be measured directly and must be inferred. Calculating the ambient supersaturation in fog requires knowledge of the aerosol hygroscopicity as well as particle size distribution, and relatively few values have been reported in the literature. Here we use κ -Köhler theory to derive aerosol activation properties based on particle hygroscopicity and dry particle size distributions, and then estimate the effective peak supersaturation during eight cases of radiative fog at the Southern Great Plains site in rural north-central Oklahoma, USA. The mean hygroscopicity parameter κ of particles likely to act as cloud condensation nuclei varied from 0.14 to 0.43. Ambient effective peak supersaturation during the fog episodes was between 0.01%–0.07%, with most values below 0.04%. The minimum 50% dry activation diameter generally ranged between 300–400 nm with little activation of particles with diameters below 300 nm.

1. Introduction

Fog is a phenomenon in which the surface layer reaches saturation and cloud droplets activate, reducing the surface visibility below 1 km, and is typically classified according to its formation mechanism. Radiation fog is caused by near-surface radiative cooling, and usually forms under nocturnal clear-sky conditions. Although other processes such as drainage flows may play a role in radiation fog formation, radiative cooling remains the dominant formation mechanism. Radiative fog is a frequent occurrence at many locations worldwide (e.g., Haeffelin et al., 2010; Izett et al., 2019; Price et al., 2018), particularly at higher latitudes between autumn and spring when the nights are longest are radiative cooling is maximized.

Understanding the formation of radiation fog as well as its microphysical characteristics is important for a number of reasons. The radiative effect of aerosols through both direct forcing and their role as condensation nuclei remains one of the greatest sources of uncertainty in global climate models (Mülmenstädt & Feingold, 2018). Fog also impacts the surface energy balance terms, and even optically thin haze can have a significant impact on the observed surface longwave radiative flux due to the strong sensitivity to even small amounts of liquid water within the infrared window at 8–13 μm (Turner & Long, 2004; Turner et al., 2007). The presence of fog can alter boundary-layer dynamics and modify the wind profile, with resulting impacts on the morning transition and subsequent CBL development, as outlined by Fitzjarrald and Lala (1989). Fog can also modulate atmospheric composition and chemistry through secondary aerosol formation, and the strong static stability during radiative fog can increase pollutant levels in the surface layer, leading to adverse health impacts (Tanaka et al., 1998). Radiative fog also has significant human impacts, as it is a hazard for air and road transport, and Gultepe et al. (2007) report that financial losses resulting from fog can rival those due to severe convective storms or winter weather.

The size distribution and concentration of aerosols are critical parameters in the life cycle of radiation fog, and also affect the supersaturation within the fog (Bott, 1991). The aerosol number concentration (N_a) largely determines the cloud droplet number concentration (e.g., Gultepe & Isaac, 1999), which in turn impacts the fog evolution and liquid water content (Jia et al., 2019; Maalick et al., 2016; Poku et al., 2019; Stolaki et al., 2015). In pristine environments where N_a is low, under supersaturated conditions all aerosols can activate into cloud droplets, and further increases in saturation will result in the growth of the activated droplets (known as the aerosol-limited regime). If N_a is higher then the formation of cloud droplets will be limited by the supersaturation (known as the updraft-limited regime) and only a fraction of the aerosols will become activated (Reutter et al., 2009). Unless in extremely remote regions, radiative fog falls in the

updraft-limited regime due to the low vertical velocities in fog. In this regime, the droplets compete for the limited available water, which suppresses both droplet growth and environmental supersaturation. This in turn impacts fog growth and development via changes to the droplet effective radius (Boutle et al., 2018; Poku et al., 2019). If N_a is sufficiently high, then hydrated aerosols can reduce visibility below 1 km even without particle activation (Kokkola et al., 2003). The decreasing trend in fog days in Europe over the past several decades is thought to be largely due to decreases in aerosol loading (Van Oldenborgh et al., 2010), the same effect has also reduced tule fog frequency in the Central Valley of California (Gray et al., 2019). Conversely, Ghude et al. (2017) suggest that increases in aerosol loading have to lead to an increasing trend in the number of fog days in Delhi, India, while Quan et al. (2021) show that increased aerosol loading has extended the lifetime of fog episodes across China by delaying dissipation.

At high humidity, aerosol particles grow via the condensation of water vapor. If the humidity is sufficiently high that the atmosphere is supersaturated with respect to water vapor, then aerosols will act as cloud condensation nuclei (CCN) and become activated into fog droplets. The condensational growth of aerosols is controlled by both the aerosol size and chemical composition, as well as the environmental saturation, as described by the well-known Köhler theory (Köhler, 1936). An extension to Köhler theory developed by Petters and Kreidenweis (2007) combined the activation characteristics of particles of a given chemical composition into a single hygroscopicity parameter, κ . Typical values of κ vary from 0.1 for more hydrophobic particles up to 1.3 for the most hygroscopic particles such as sea salt. The resulting theory is known as κ -Köhler theory, and it predicts the growth of a dry particle of a given size with known hygroscopicity under varying saturation levels (see Section 2.2 for more details). For particles of a known dry size and κ , κ -Köhler theory allows calculation of the critical supersaturation (SS_{crit}) above which the particle will become activated. Supersaturation fluctuates with temperature, and a particle will only become activated into a fog droplet if it remains within supersaturated air for a sufficiently long time (see e.g., Prabhakaran et al., 2020; Richter et al., 2021). The effective peak supersaturation (SS_{peak}) is the highest supersaturation that a particle experiences for a sufficiently long time such that any particles with SS_{crit} below SS_{peak} will activate (Hammer et al., 2014). Equivalently, for a given κ and SS_{crit} pair, there exists a critical diameter (or activation diameter) D_{crit}^{dry} for which all particles with dry diameter $D_{dry} > D_{crit}^{dry}$ will activate. Through Köhler theory we can also define the particle wet activation or critical diameter, D_{crit}^{wet} , which is the particle diameter at SS_{crit} . While the particle diameter remains below D_{crit}^{wet} , the particle is in stable equilibrium and remains unactivated.

Aerosol activation in fog has also been investigated in terms of nucleation scavenging. Nucleation scavenging is used to describe the removal of aerosols from the ambient particle size distribution as they become activated and grow into fog droplets. Aerosols can additionally be removed by collision-coalescence processes, or through collection by other fog droplets (impaction scavenging). Both nucleation and impaction scavenging may lead to subsequent sedimentation or “wet removal” of aerosols. The hygroscopicity of the remaining interstitial aerosols can also potentially be altered via preferential scavenging of more highly hygroscopic particles (Collett et al., 2008). In fog, nucleation scavenging dominates over impaction scavenging due to the relatively small size of activated fog droplets limiting the swept area.

Characterizing aerosol activation in fog is important for the understanding of cloud microphysical processes more generally, as well as for developing physically realistic parameterization schemes for numerical weather prediction and large-eddy simulation models. Several typical aerosol activation schemes widely used in numerical models are based on the assumption that saturation is reached through adiabatic ascent, and include a vertical velocity threshold to account for sub-grid ascent (Poku et al., 2021). These schemes, however, have been shown to produce an excessively high number of fog droplets, artificially lowering the fog droplet effective radius, thus leading to unphysically strong radiative cooling at the fog top (Boutle et al., 2018); recent work has suggested that fog simulations may require aerosol activation schemes in which saturation can be achieved through non-adiabatic processes (Poku et al., 2021).

In this regard, several field campaigns have investigated aerosol activation and nucleation scavenging during fog events, generally with a focus on either the variation of scavenging rates across chemical species or the effect of particle size on scavenging rates. It follows from κ -Köhler theory that if κ does not vary with particle size, the largest particles will have the lowest SS_{crit} and will activate first as the supersaturation increases. However the activation characteristics of CCN depend not only on their size but also their chemical

composition, and previous work has shown that hygroscopicity is usually size dependent (e.g., Hammer et al., 2014), with smaller particles generally being less hygroscopic.

Noone et al. (1992) showed that particles with diameters above 700 nm were efficiently scavenged in fog in the Po Valley in Italy, while particles with diameters below 300 nm were not affected. Further work in the same region by Gilardoni et al. (2014) examined size-dependent nucleation scavenging during 14 fog events, finding that the scavenging efficiency for particles larger than 700 nm varied between 40%–86% across the events, and there was virtually no scavenging of particles below 100 nm. Gilardoni et al. (2014) also examined how the scavenging rate varied across chemical species during these events, finding mass scavenging rates varying from as high as 70% for nitrate to 39% for black carbon. Nucleation scavenging in fog (in terms of aerosol activation properties) has also been investigated at the SIRTAsite near Paris, France by Hammer et al. (2014) and Mazoyer et al. (2019). Both studies showed that aerosols at that site were characterized by low hygroscopicity due to anthropogenic effects such as traffic emissions and wood burning, with an average κ value of 0.14–0.17. The derived κ values were used to calculate $D_{\text{crit}}^{\text{dry}}$, $D_{\text{crit}}^{\text{wet}}$ and SS_{peak} during fog. Hammer et al. (2014) showed that the average $D_{\text{crit}}^{\text{wet}}$ was highly variable across 17 fog events, with values ranging between 1 and 5 μm and an average value of 2.6 μm . Further analysis of 23 fog events by Mazoyer et al. (2019) found the average $D_{\text{crit}}^{\text{dry}}$ to be 390 nm, $D_{\text{crit}}^{\text{wet}}$ to be 3.8 μm , and SS_{peak} to be 0.043%. A similar analysis by Shen et al. (2018) at Wuqing, a rural area in the North China Plain, during the HaChi (Haze in China) campaign found a size-dependent value of κ of between 0.25 and 0.3, which resulted in supersaturations between 0.01% and 0.05% for three fog cases. The same technique has also been applied by Ziková et al. (2020) to examine aerosol activation in stratus fog at Milešovka observatory, a remote and elevated site in the Czech Republic, finding an average $D_{\text{crit}}^{\text{dry}}$ over 14 stratus fog episodes of 200 nm.

Here, we examine aerosol activation during eight cases of radiative fog at a site in rural north-central Oklahoma. The size-dependent hygroscopicity parameter (κ) is determined for each fog event. The derived κ values are compared to those from previous studies, including from sites with a stronger anthropogenic influence. κ -Köhler theory is then applied to calculate $D_{\text{crit}}^{\text{dry}}$, $D_{\text{crit}}^{\text{wet}}$ and SS_{peak} . Section 2 describes the site and instrumentation and explains the method used to calculate the aerosol hygroscopicity, wet and dry activation diameters, and supersaturation. Section 3 gives an overview of all the cases analyzed and presents the derived hygroscopicity, aerosol activation parameters, and supersaturation. Conclusions are given in Section 4.

2. Data and Methods

2.1. Site and Instrumentation

The Department of Energy Atmospheric Radiation Measurement (ARM) Southern Great Plains (SGP) site is located in Lamont, Oklahoma, USA (36.607°N, 97.488°W, 314 m AMSL). The surrounding area is comprised of grassland and rangeland. The immediate surroundings are rural and the closest large urban areas are Oklahoma City (130 km south, 640,000 residents), and Wichita (100 km north, 390,000 residents). The ARM SGP atmospheric observatory hosts a suite of in situ and remote sensing instrumentation designed to study cloud, aerosol, and atmospheric processes. An overview of the site can be found in Sisterton et al. (2016).

The instrumentation at the SGP site includes a dedicated atmospheric observing system (AOS), which measures a variety of aerosol characteristics, including the size distribution at ambient humidity for particle aerodynamic diameters between 487 nm and 19.8 μm , and the size distribution at dry humidity for particles between 106 and 514 nm. A history of the AOS and details of each of the instruments contained in the system as well as the data they provide can be found in Uin et al. (2019), and a brief description is included here for completeness. Aerosols sampled by the AOS are drawn through an inlet at a height of 10 m. The air is sampled through a 20-cm diameter pipe at a flow rate of 1,000 L min^{-1} . A flow distributor samples 150 L min^{-1} of the flow and splits it into five separate lines of 30 L min^{-1} before it is passed to the instrumentation. Schematics of the instrument setup used in the AOS can be found in Figure 4 of Uin et al. (2019). Details of the instrumentation used for this study can be found in Table 1.

The AOS includes an aerodynamic particle sizer (APS), which measures the particle size distribution across 53 size bins for particles with an aerodynamic diameter between 487 nm and 19.8 μm . The flow is not dried

Table 1
Instrumentation at the Southern Great Plains Site Used in This Study

Instrument	Abbreviation	Manufacturer and model	Measured parameters	Time resolution
Humidified tandem differential mobility analyzer	HT-DMA	Brechtel Manufacturing 3002	Size-resolved growth factor	6.3 min per dry size, 31.6 min per full cycle
Aerosol particle sizer	APS	TSI 3321	Particle size distribution (ambient; diameter 487 nm–19.8 μm)	1 s
Scanning mobility particle sizer	SMPS	TSI 3936	Particle size distribution (dried; diameter 106–514 nm)	5 min
Condensation particle counter	CPC	TSI 3772	Number concentration >10 nm	1 s
Cloud condensation nuclei counter	CCN counter	Droplet Measurement Technologies CCN-200	Droplet concentration (SS = 0–1.0%)	10 min per SS, 1 hr for full cycle
Present weather detector	PWD	Vaisala PWD22	Visibility	1 min
Ceilometer	-	Vaisala CL31	cloud base height, vertical visibility	16 s

prior to entering the APS, although there may be changes in the flow temperature and humidity (compared to environmental conditions outside the AOS) due to passage through the inlet and into the APS. In the remainder of the paper, we describe the APS PSD as representative of ‘ambient’ humidity to delineate it from the dry PSD measured by other instruments, but it should be noted that the APS PSD may differ slightly from that measured at true ambient humidity. The flow is also sampled by a cloud condensation nuclei counter (CCNc). The CCNc is operated in a two-column configuration (Uin, 2016), with one column measuring the activated particles at a constant supersaturation of 0.4% and the second column measuring activated particles while cycling through supersaturation values of 0%, 0.1%, 0.2%, 0.4%, 0.8%, and 1.0%. Each full cycle takes approximately one hour. Another sample line dries the flow to a low relative humidity using a Nafion dryer before the sample is passed onto a scanning mobility particle sizer (SMPS), which provides the dried particle size distribution for diameters between 106–514 nm. The AOS also includes a humidified tandem differential mobility analyzer (HT-DMA). The HT-DMA first dries the sample before aerosols of a given size (50, 100, 150, 200, and 250 nm) are selected. The dry monodisperse aerosols are then humidified (to a known humidity) and the resulting particle size distribution is measured. The AOS also includes a condensation particle counter (CPC), in which the sampled aerosol is dried with a Nafion dryer before being mixed with supersaturated butanol vapor and cooled. Particles that grow via condensation are counted to provide the aerosol concentration. The fine mode CPC used here has a lower detection limit of 10 nm.

The sample flow is not dried prior to entering the APS, and so the APS data represents the hydrated particle (and droplet) size distribution at approximately ambient relative humidity, although as noted previously this may differ slightly from the true ambient particle size distribution due to changes in temperature or humidity along the flow path inside the AOS. Fog droplets are clearly visible in the APS data (see Figure 1b). While previous investigations have shown that the AOS inlet system has transmission efficiency of 1 for droplets between 10 nm and 4 μm (Bullard et al., 2017), there was uncertainty of over 50% in the transmission efficiency for droplets larger than 4 μm due to the low particle counts at this size during the inlet characterization experiment. For this reason, we do not quantify the fog droplet concentration. There is no impactor upstream of the APS, so all fog droplets that are transmitted through the AOS will be included in the APS data unless they are larger than the maximum droplet size recorded by the APS ($\approx 20 \mu\text{m}$).

The data recorded by the SMPS is subsampled from the same intake flow as the APS, but the flow is dried with a Nafion dryer prior to entering the SMPS (Uin et al., 2019). Here we refer to the particle size distribution (PSD) recorded by the SMPS as the dry PSD, and the PSD from the APS as the ambient PSD (i.e., the APS flow is not dried). The largest bin size in the SMPS is 470 nm and so dry particles with diameters >470 nm are not included in the data. As there is no impactor on the droplets at ambient size, in theory, the dry PSD could contain fog droplet residuals as well as interstitial particles. Unlike in some previous studies on aerosol activation in fog, there is no counterflow gradient virtual impactor included in the instrumentation, and so droplets and interstitial particles are not directly separated. However, the strong reduction in dried particles of larger sizes in the SMPS data during the fog event (e.g., Figure 1c), and the monotonic

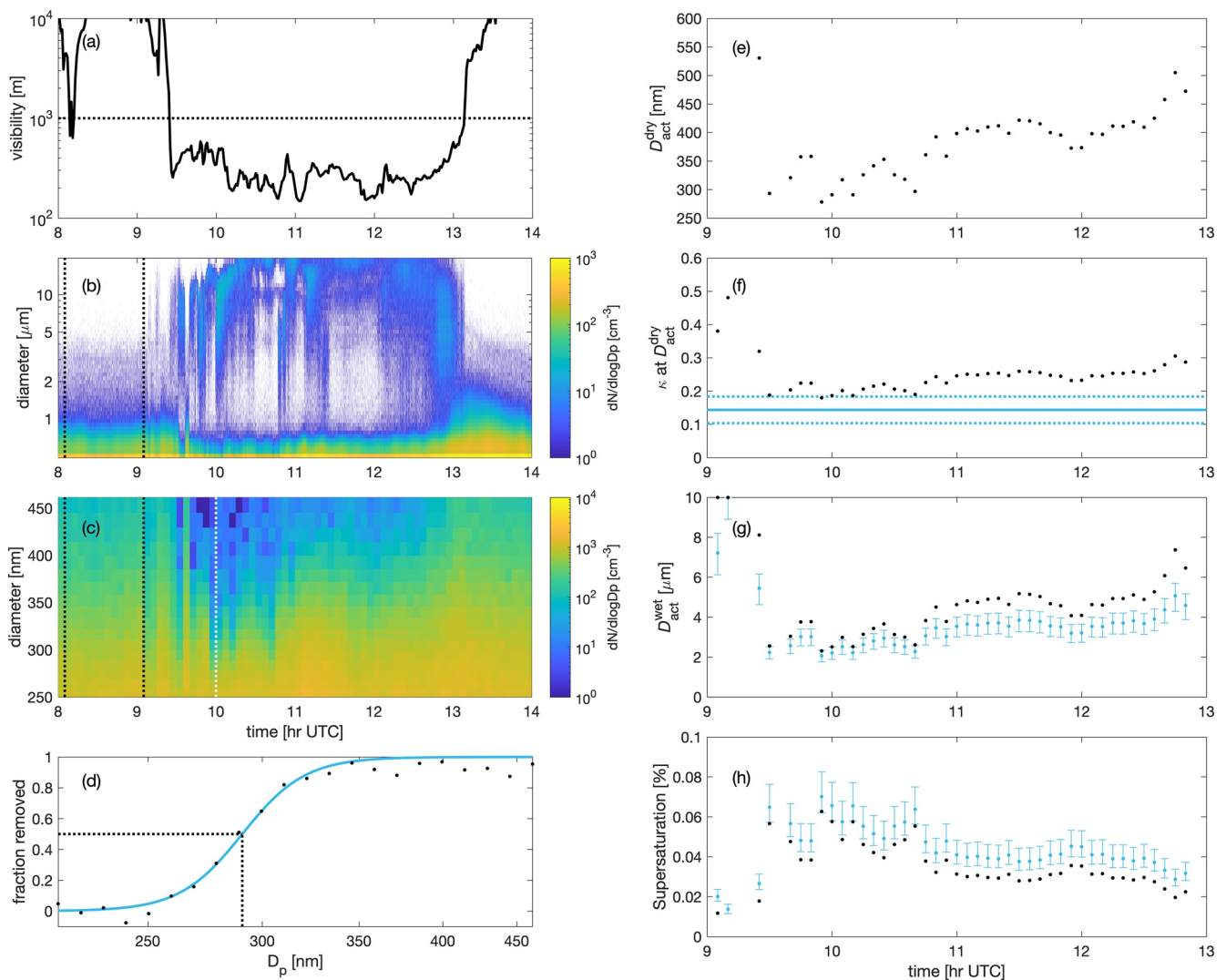


Figure 1. Example case during fog on 2019/08/04. (a) time series of visibility at 2 m height, with the black dashed line indicating the fog threshold at 1 km, (b) particle size distribution (PSD) at ambient humidity, (c) dry PSD. The black dashed lines in (b) and (c) show the pre-fog time period used to characterize the dry PSD. (d) the size-dependent scavenging of particles (black dots) at 10 UTC (white line in c) and the corresponding hill fit. The black dashed line shows the 50% scavenging diameter (D_{act}^{dry}). (e) Time-varying D_{act}^{dry} , (f) κ at D_{act}^{dry} (black dots), $\kappa_{SS=0.1\%}$ (solid line), and κ_{upper} and κ_{lower} (dashed lines). (g) D_{act}^{wet} calculated from D_{act}^{dry} using κ (black dots), $\kappa_{SS=0.1\%}$ (black dots), and κ_{upper} and κ_{lower} (error bars). (h) Supersaturation required to produce D_{act}^{wet} in (g).

relationship between the fraction of particles removed and the particle diameter (as seen in Figure 1d) indicates that we see the removal of particles in the dry PSD due to nucleation scavenging in the fog. This suggests that either some fog droplets are lost in the AOS inlet or tubing, in which case they would not be present in either the ambient PSD or dry PSD; or there may be attrition of supermicron fog droplets during the drying process. The AOS at the SGP site conforms to the standard NOAA/ESRL federated aerosol network inlet configuration, and theoretical particle passing efficiency calculations for this configuration indicate a 99% passing efficiency for 1–2 μm diameter particles, falling to 50% for particles of diameter 7–11 μm (Andrews et al., 2019). As mentioned previously, low droplet counts at diameters >4 μm during the aerosol inlet characterization experiment led to >50% uncertainty in the experimentally determined passing efficiency for particles above that size (Bullard et al., 2017). We assume here that any fog droplet residuals included in the dry PSD would be drawn from across the range of diameters of particles that activate during the fog event, causing the activation diameter to be unbiased.

Aside from the aerosol measurements, the surface meteorology data at the SGP site also provides standard meteorological variables such as temperature, relative humidity, and precipitation rate, and a present

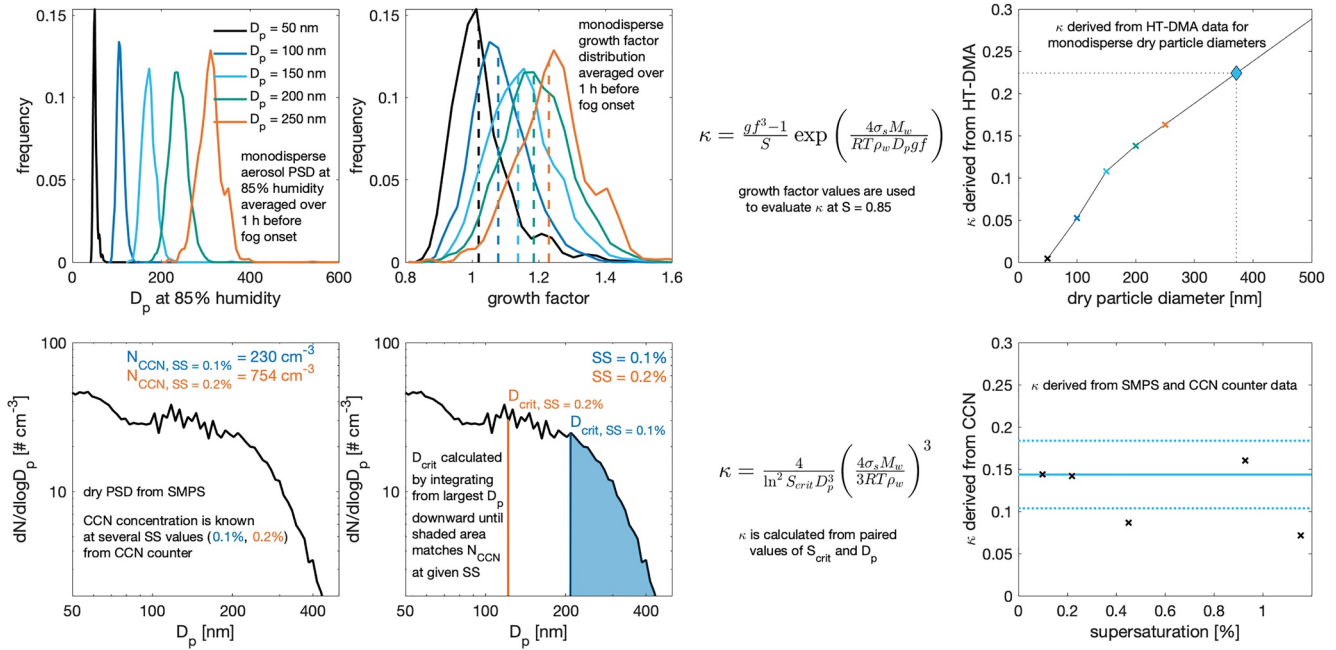


Figure 2. Schematic demonstrating how κ is derived, showing sample data from 2019/08/04. The top row shows how κ is derived from humidified tandem differential mobility analyzer measurements of monodisperse particle growth. The upper right panel shows κ extrapolated to an example D_{dry} of 375 nm (black diamond). The bottom row shows how κ is derived from the cloud condensation nuclei counter and scanning mobility particle sizer measurements. The lower right panel shows κ at a range of supersaturation values (black crosses), and the solid black line shows κ calculated at $SS = 0.1\%$, and the dashed lines show $\kappa \pm \delta\kappa$, where $\delta\kappa = 0.04$. More details on both methods can be found in the text.

weather detector (PWD) records horizontal visibility at 1 and 10 min averaging times. A ceilometer measures cloud base height and vertical visibility.

2.2. Deriving the Particle Hygroscopicity

Two methods are used to calculate the particle hygroscopicity, κ . Both methods involve the application of κ -Köhler theory (Petters & Kreidenweis, 2007), which links particle condensational growth under varying saturation levels to κ via the following equation:

$$S(D) = \frac{D^3 - D_d^3}{D^3 - D_d^3(1 - \kappa)} \exp\left(\frac{4\sigma_s M_w}{RT\rho_w D}\right), \quad (1)$$

where D_d is the dry particle diameter, D is the particle diameter at saturation ratio S , κ is the hygroscopicity, σ_s is the surface tension of the solution droplet (here taken as the surface tension of a pure water droplet), M_w is the molar mass of water, R is the universal gas constant, T is the air temperature, and ρ_w is the density of water. Equation 1 can also be used to evaluate the supersaturation SS , which is equivalent to $100(S-1)$.

The first method for deriving κ is based on the HT-DMA measurements, which are available for five of the case studies. The HT-DMA system uses two differential mobility analyzers. The aerosol sample is dried using a Nafion dryer, and then the first DMA is used to select monodisperse aerosols with dry diameters of 50, 100, 150, 200, and 250 nm in turn. The monodisperse aerosols are exposed to 85% relative humidity in a humidification system, and the second DMA is used in combination with a CPC to measure the size distribution of the humidified particles. Example data are shown in the upper left panel of Figure 2. The size-resolved particle growth factor (gf) can be derived by comparing the dry particle size to the humidified particle size distribution, as shown in the upper center panel of Figure 2, where the mean growth factor for each particle size is marked by the dashed vertical lines. The mean growth factor can then be used to derive κ for each dry particle size using the equation in the upper row of Figure 2 and setting S as 0.85 and D_p as the dry particle diameter (this equation is a rearranged form of Equation 1). As the largest size dry particle selected in the HT-DMA is 250 nm, assumptions are required to estimate κ at particle diameters larger than 250 nm.

We extend κ beyond a dry particle diameter of 250 nm by extrapolating based on the derived values of κ at 200 and 250 nm, following Mahish et al. (2018). The black diamond in the upper right panel of Figure 2 illustrates this extrapolation for a sample dry particle diameter of 375 nm (in this case, κ at 375 nm is 0.22).

The second method for deriving κ relies on a combination of the dry particle size distribution and CCN counter measurements, and is illustrated in the bottom row of Figure 2 using sample data from 2019/08/04. The CCN counter measures the number of activated droplets at six supersaturation values between 0% and 1.0%. Sample values for supersaturations of 0.1% and 0.2% are shown in the lower left panel of Figure 2. For each CCN measurement, the dry particle size distribution from the SMPS (black line in the bottom row of Figure 2) is cumulatively summed, starting from the largest particle size and working downwards, until the number of activated droplets matches that measured by the CCN counter. This is illustrated for the 0.1% and 0.2% supersaturation CCN counts in the lower center panel of Figure 2, where the vertical lines mark the diameter where summing the SMPS distribution to the right of the black and orange lines provides the corresponding N_{CCN} values shown in the leftmost panel. The diameter at which the concentrations are matched is designated $D_{\text{crit}}(\text{SS})$, such that

$$N_{\text{CCN}}(\text{SS}) = \int_{D_{\text{crit}}(\text{SS})}^{\infty} N(D_p) dD_p. \quad (2)$$

The supersaturation in the CCN counter is recalculated using a parameterization based on the inner wall temperature following Lance et al. (2006). Since the supersaturation at which each activated droplet concentration occurred is known, κ can then be calculated via

$$\kappa = \frac{4}{\ln^2 S_{\text{crit}} D_p^3} \left(\frac{4\sigma_s M_w}{3RT\rho_w} \right)^3 \quad (3)$$

(Petters & Kreidenweis, 2007). This method assumes a sharp cut-off diameter delineating activated and unactivated particles, that is, that the particle activated fraction is 0 for $D_p < D_{\text{crit}}(\text{SS})$ and 1 for $D_p \geq D_{\text{crit}}(\text{SS})$. The aerosol hygroscopicity as a function of supersaturation at the SGP site, calculated using the method outlined above, has recently been released as an ARM program value added product named CCNSMPKAPPA (Kulkarni et al., 2021). The CCN counter operates at nominal supersaturation values of 0%, 0.1%, 0.2%, 0.4%, 0.8%, and 1.0%, but κ is not calculated at a supersaturation of 0% due to S_{crit} being in the denominator of Equation 3. We apply the value of κ found at the lowest supersaturation of 0.1%, although the supersaturation in fog is typically less than 0.1% (Hammer et al., 2014; Hudson, 1980; Mazoyer et al., 2019; Shen et al., 2018). We did test the procedure outlined in Mazoyer et al. (2019), which fits a linear model to κ and SS, and then evaluates this at $\text{SS} = 0.05\%$. However, we found at most a 0.04 increase in κ using this method, which is comparable to the uncertainty associated with the supersaturation of the CCNc. As such, we calculated the supersaturation using the κ value calculated at $\text{SS} = 0.1\%$ ($\kappa_{\text{SS} = 0.1\%}$), and examined the effect of uncertainty in κ by using $\kappa = \kappa_{\text{SS} = 0.1\%} \pm \delta\kappa$, with $\delta\kappa = 0.04$ (for simplicity we label $\kappa = \kappa_{\text{SS} = 0.1\%} + \delta\kappa$ as κ_{upper} and $\kappa = \kappa_{\text{SS} = 0.1\%} - \delta\kappa$ as κ_{lower}), as shown in Figure 2b.

Both methods for deriving κ are illustrated in Figure 2 for a fog case that occurred on August 4, 2019. Both methods characterize κ based on data averaged over one hour prior to the fog onset, indicated by the vertical black lines in Figures 1b and 1c. The upper row of Figure 2 demonstrates the method for deriving κ from the HT-DMA measurements. The black crosses on the right panel show the derived κ values for the five dry particle sizes used in the HT-DMA, and the black diamond shows the extrapolated κ value for a dry particle diameter of 375 nm.

Meanwhile the method for deriving κ based on the CCN counter and SMPS measurements is shown in the lower row of Figure 2. Here the black crosses in the lower right panel of Figure 2 show the variation of κ with supersaturation as derived from the SMPS and CCN counter data, provided by the ARM value-added product CCNSMPKAPPA. Although the CCN counter operates at target supersaturations of $\text{SS} = 0.1\%$, 0.2%, 0.4%, 0.8%, and 1.0%, the supersaturation is recalibrated based on the CCN counter inner wall temperature following Lance et al. (2006), which is why the supersaturation values are shown in Figure 2 differ from the target values. We evaluate κ at the lowest supersaturation value of $\text{SS} = 0.1\%$. The effect of uncertainty in κ on droplet activation is examined by testing $\kappa_{\text{SS} = 0.1\%} \pm \delta\kappa$ with $\delta\kappa = 0.04$ as described above. For

Table 2
Fog Cases From the Southern Great Plains Site

Date	Start time [LT]	Duration [hours]	Median (minimum) 10-min visibility [m]	T [°C]	Wind speed [m s ⁻¹]
2017/04/18	03:14	2.5	387 (238)	12.0	2.7
2017/12/18	05:17	5.0	276 (168)	0.5	2.9
2018/11/30	22:38	9.2	345 (45)	4.6	2.3
2018/12/01	02:38	2.0	305 (174)	7.7	3.4
2019/08/04	04:27	3.8	258 (161)	21.7	1.2
2019/09/14	06:17	2.6	471 (278)	19.9	2.2
2019/12/22	00:40	4.5	498 (142)	1.7	3.6
2019/12/23	04:08	4.3	287 (159)	-2.6	2.2

the case shown in Figure 2, this gives $\kappa_{SS=0.1\%} = 0.14$, $\kappa_{lower} = 0.10$, and $\kappa_{upper} = 0.18$. Further details on how both methods are applied to the data are given in Section 2.3.

2.3. Data Processing

We are ultimately interested in the activation and nucleation scavenging of aerosols in radiative fog. Cases of fog during 2017–2019 were identified by a preliminary screening based on horizontal visibility data, using a 1 km threshold. Cases of precipitation fog or stratus lowering fog were removed by inspecting backscatter profiles from a ceilometer that is collocated at the SGP site. Cases were also restricted to those where the SMPS data and at least one of either the HT-DMA or CCN counter were available so that κ could be quantified. This screening resulted in eight radiative fog cases. Details of each case are listed in Table 2.

While the start and end time of the fog episode can be assessed based on the horizontal visibility reported by the PWD (this is how the fog start time and duration reported in Table 2 is determined), this represents the visibility at a height of 2 m. The inlet used in the AOS draws samples at a height of 10 m, and so there are times during shallow fog when the visibility is below 1 km at 2 m but the fog does not reach the height of the AOS inlet. For this reason, we identify the start and end time of the fog at 10 m based on an increase in the supermicron droplet concentration in the APS data (see Figure 1b).

The aerosol dry size distribution and hygroscopicity are characterized using data averaged across a 1-hr period prior to the fog onset, as in Mazoyer et al. (2019). The dried particle size distribution recorded by the SMPS during the fog event is then compared to that from before the fog started to examine the size-dependent activation/nucleation scavenging of particles during the fog, following the method of Hammer et al. (2014). This is illustrated for an example case from 2019/08/04 in Figure 1. The black dashed lines in Figures 1b and 1c indicate the start and end of the time period used to characterize the aerosol PSD and hygroscopicity prior to the fog onset (we refer to this averaged aerosol PSD as the pre-fog PSD). The white dashed line at 10 UTC in Figure 1c is during the fog event. By comparing the average particle size distribution between the two black lines (pre-fog PSD) to that at the white dashed line (during fog), we can see what fraction of particles of different sizes have been removed via nucleation scavenging, as shown in Figure 1d. We apply a sigmoid fit to the fraction of particles removed and define the diameter where 50% of the particles are removed (i.e., the median activation diameter) as D_{act}^{dry} . For the particle size distribution at 10 UTC shown in Figure 1d, D_{act}^{dry} occurs at 290 nm.

We can then apply Equation 1 using the values of κ determined as described in Section 2.2. By setting D_{act}^{dry} as D_d and varying D across a range of ambient diameters, SS_{crit} and D_{act}^{wet} can be found as the value where SS is maximized and the diameter where this occurs. As the dry particle size distribution varies over the course of the fog event, we recalculate D_{act}^{dry} following the method illustrated in Figure 1d every 5 min based upon the SMPS data time resolution. This is demonstrated in Figure 1e, which shows the variation of D_{act}^{dry} over time during the fog on 2019/08/04. As the size-resolved κ generated using the HT-DMA data is extrapolated to D_{act}^{dry} , this also varies in time (black dots in Figure 1f), while the κ values generated from the CCN counter and SMPS data ($\kappa_{SS=0.1\%}$, solid black line; κ_{lower} and κ_{upper} , dashed black lines in Figure 1f) are treated as constant across the fog event. Based on the κ values shown in Figure 1f, D_{act}^{wet} and SS_{peak} are then calculated (Figures 1g and 1h). D_{act}^{wet} can be considered the delineation diameter between hydrated and activated particles.

3. Results and Discussion

Some general characteristics of the fog events are listed in Table 2 and illustrated in Figure 3. The cases encompass a wide range of temperatures, from -2°C to 21°C . Each of the fog events started during the night when radiative cooling rates are maximized and the fog duration varied between 2 and 9 hr. The fog ended before sunrise in half of the cases, and in three cases the fog persisted for almost two hours beyond

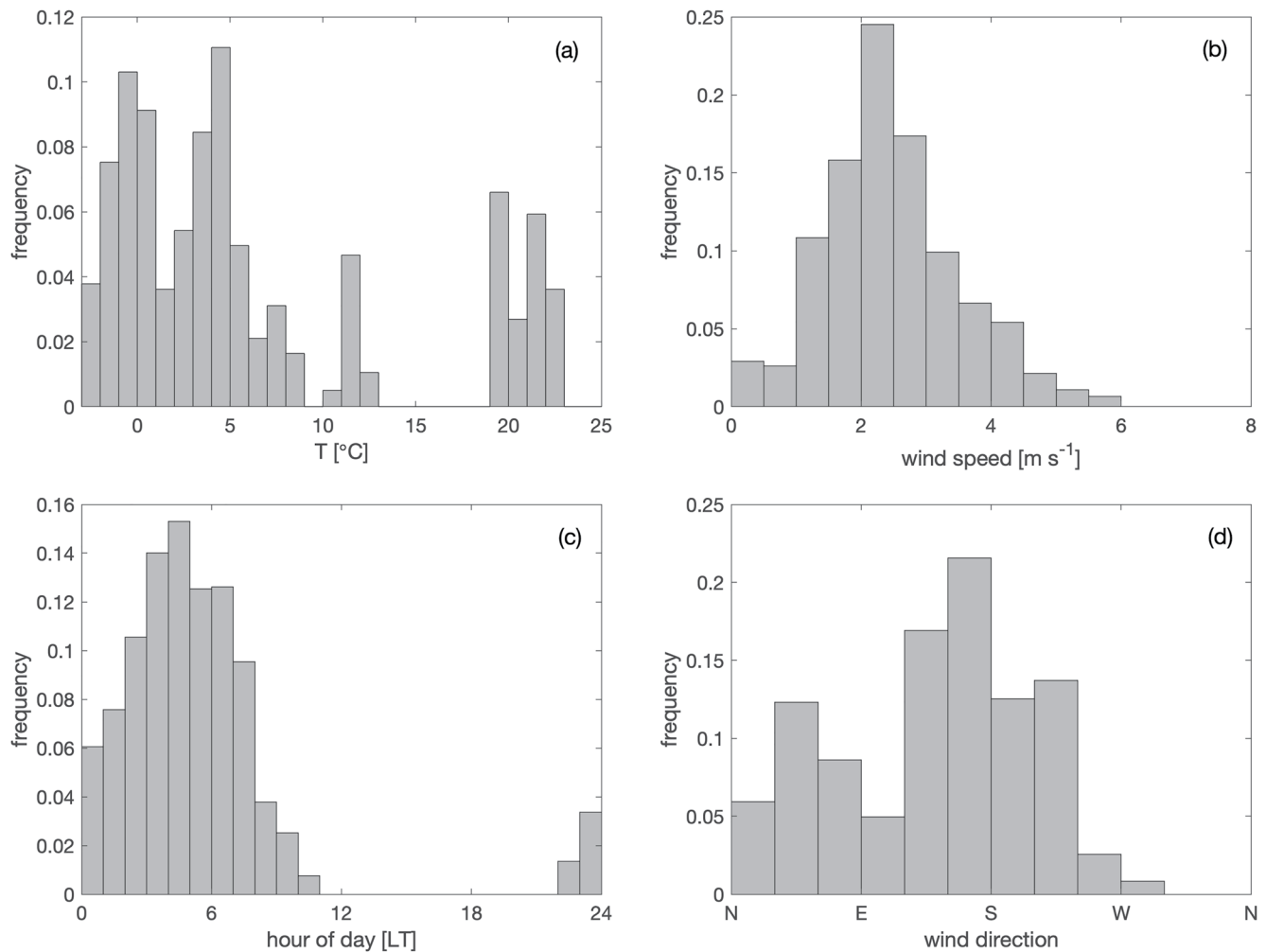


Figure 3. Histograms of several variables during the fog cases (a) the 2-m air temperature; (b) wind speed; (c) time of day (local time); (d) wind direction.

sunrise. The mean wind speed was below 4 m s^{-1} for all cases (Table 2), as is typical for radiation fog. The fog start time and duration reported in Table 2 are based on the horizontal visibility at 2 m height. However, as mentioned above the AOS inlet is at a height of 10 m, and so fog may be present at 2 m but not reach a height of 10 m. This is illustrated in Figures 4 and 5, which show the particle size distribution from the APS and the SMPS, respectively. The vertical black lines in Figures 4 and 5 indicate the start and end time of the fog based on a 1 km horizontal visibility threshold at 2 m height. There is clearly a large variability between the cases; in some cases such as 2017/12/18 and 2019/08/04, the decrease in visibility at 2 m coincides with the increase in the concentration of supermicron fog droplets, while in other cases such as 2018/12/01 and 2019/12/23 the visibility decreases below 1 km at 2 m height several hours before an increase in the presence of supermicron droplets at 10 m. This indicates that in some cases the fog may remain shallow for several hours while sometimes it may grow vertically (and thus be more likely to transition to optically thick) quite rapidly. Even using horizontal visibility measurements from 2 m height may miss cases of very shallow fog, as discussed by Izett et al. (2019).

The derived hygroscopicity parameters for each of the fog cases are presented in Table 3. κ derived from the HT-DMA measurements is presented at a constant dry activation diameter of 400 nm to allow for easy comparison between the cases, although for the analysis it is extrapolated to $D_{\text{act}}^{\text{dry}}$ as indicated in Figures 1e and 1f. In general, the κ values across all the fog cases are similar to κ reported in previous studies for continental aerosols (e.g., Gilardoni et al., 2014; Phillips et al., 2018). Some areas with strong anthropogenic influences on the aerosol composition, such as from traffic emissions, have been shown to have lower κ , for

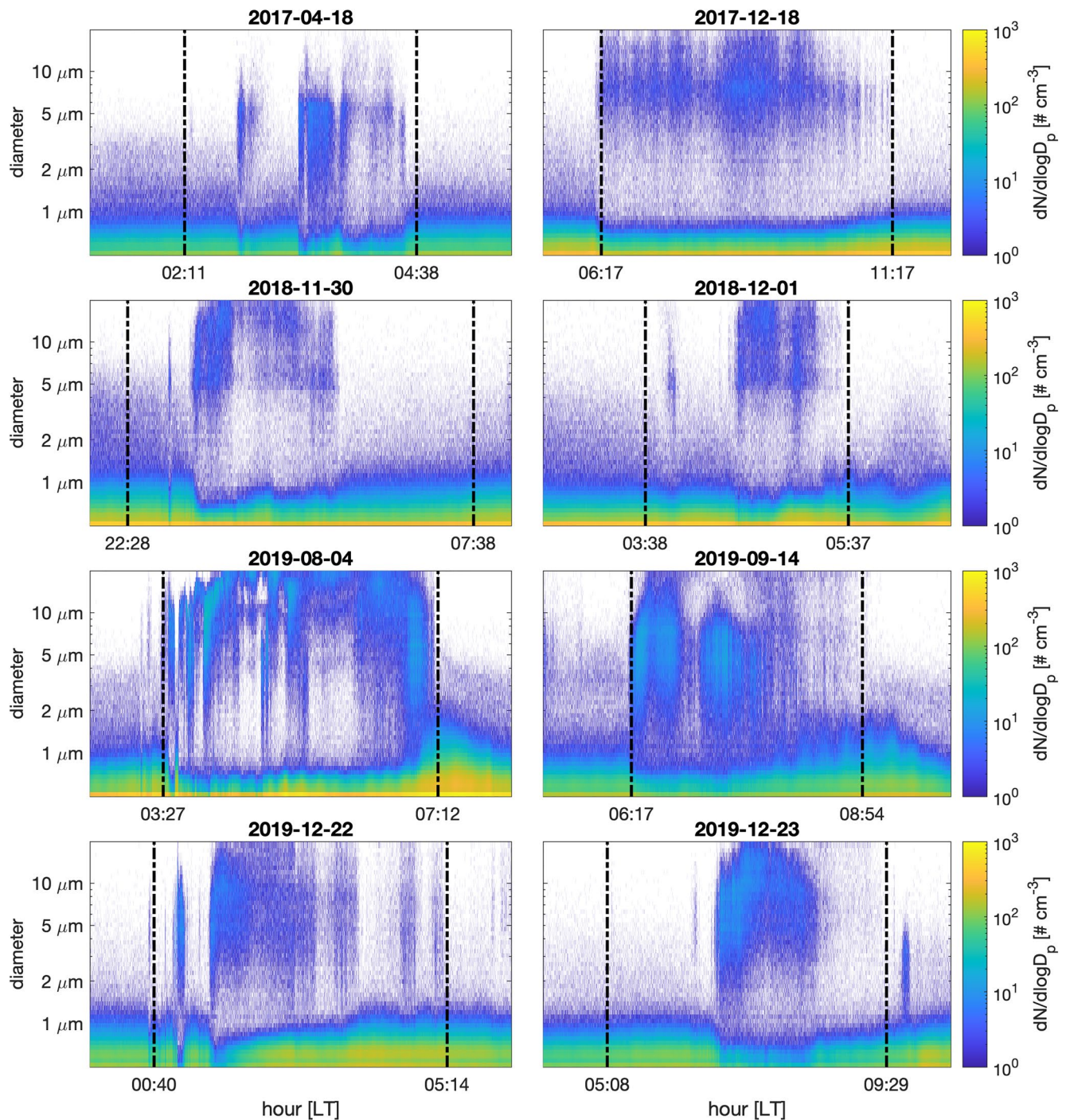


Figure 4. Particle size distributions using the aerodynamic particle sizer data from the fog cases. The vertical black lines indicate the start and end of the fog diagnosed based on the visibility at 2 m.

example, the average κ at the SIRTA site close to Paris is in the range 0.14–0.17 (Hammer et al., 2014; Mazoyer et al., 2019). The two instances of radiation fog that occur during the summer and early autumn show lower κ values ($\kappa_{SS=0.1\%} = 0.14, 0.17$). These lower κ values are closer in line with those found by Hammer et al. (2014) and Mazoyer et al. (2019), although the decrease in κ at the SGP site in summer is more likely due to the increased presence of secondary organic aerosol of biogenic origin, which is less hygroscopic (Jefferson et al., 2017; Parworth et al., 2015).

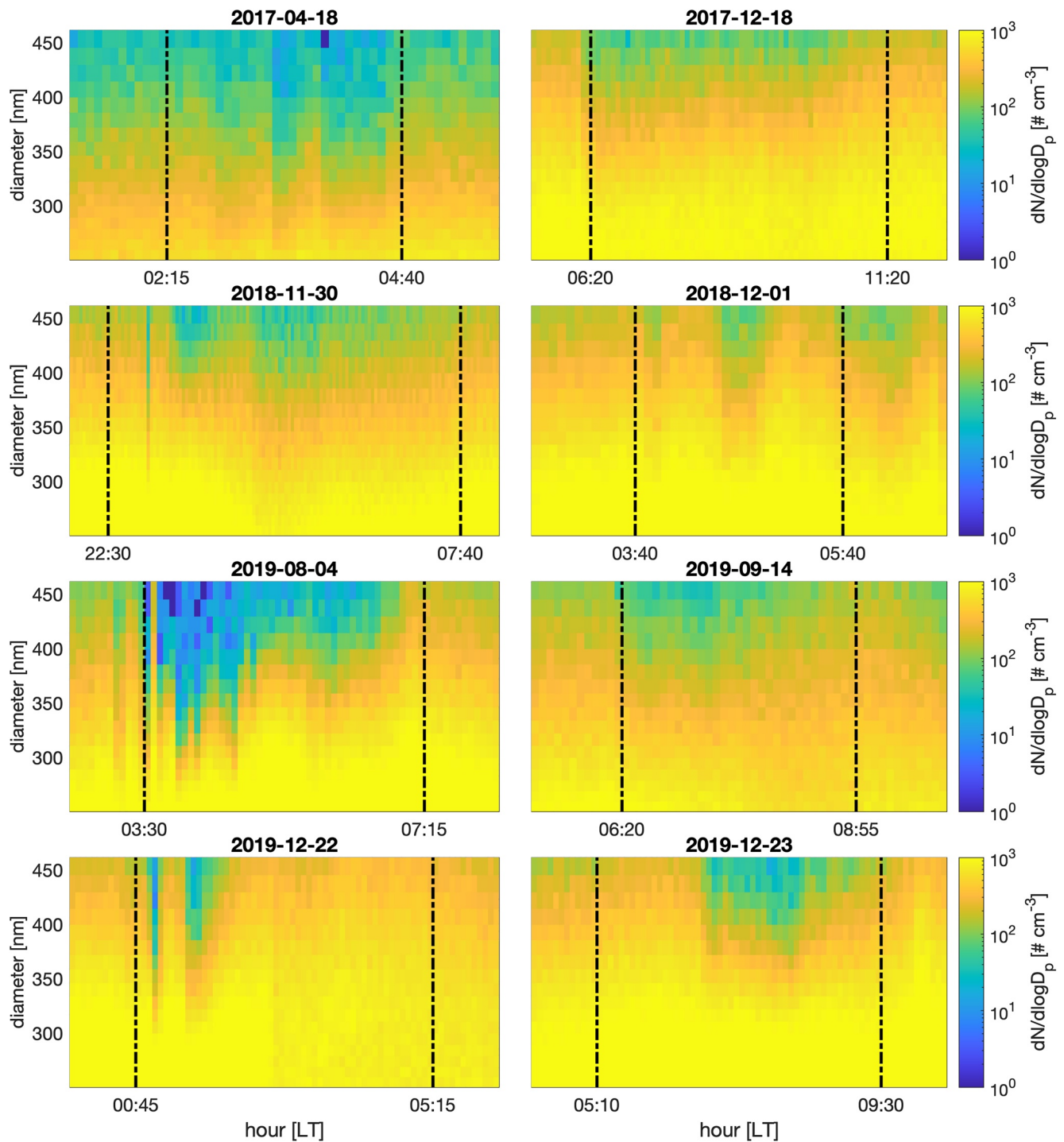


Figure 5. As for Figure 4, but showing the corresponding dry particle size distribution measured by the scanning mobility particle sizer.

Previous work at the SGP site calculated the hygroscopic growth of particles based on 7 years of aerosol scattering data, finding that hygroscopic growth rates at this site are slightly higher in winter and spring (when most of the fog cases occur) due to higher nitrate mass fractions during these seasons (Jefferson et al., 2017). This is also reflected in the cases shown in Table 3, where the lowest κ values are seen during the cases in summer and early autumn (2019/08/04 and 2019/09/14). The diurnal and annual pattern in aerosol hygroscopicity at the SGP site across a range of particle sizes was also investigated by Mahish and

Table 3
Activation Properties During Each Fog Case

Date	$\kappa_{400\text{nm}}$	$\kappa_{SS=0.1\%}$	$\kappa_{\text{lower}}, \kappa_{\text{upper}}$	N_a [cm^{-3}]	Minimum $D_{\text{act}}^{\text{dry}}$ [nm]	Maximum SS_{peak} [%]		
						$\kappa_{400\text{nm}}$	$\kappa_{SS=0.1\%}$	$\kappa_{\text{lower}}, \kappa_{\text{upper}}$
2017/04/18	-	0.25	0.21, 0.29	2,880	347	-	0.039	0.042, 0.036
2017/12/18	-	0.28	0.24, 0.32	2,210	378	-	0.032	0.034, 0.030
2018/11/30	-	0.47	0.43, 0.51	4,050	374	-	0.025	0.026, 0.024
2018/12/01	-	0.23	0.19, 0.27	3,750	448	-	0.027	0.030, 0.025
2019/08/04	0.24	0.14	0.10, 0.18	2,830	278	0.063	0.070	0.083, 0.062
2019/09/14	0.36	0.17	0.13, 0.21	3,430	387	0.028	0.039	0.044, 0.035
2019/12/22	0.54	-	-	1,510	305	0.035	-	-
2019/12/23	0.46	0.34	0.30, 0.38	2,820	346	0.030	0.033	0.035, 0.031

Collins (2017). It was found that κ generally increased with increasing particle size, as seen at other sites (e.g., Hammer et al., 2014; Phillips et al., 2018), except at the smallest particle sizes where κ was affected by new particle formation events. A diurnal trend in κ was also seen across all particle sizes, with higher κ values during the daytime than at night and a peak around 15 LT. Similar to Jefferson et al. (2017), Mahish and Collins (2017) also note increases in κ during winter at larger particle sizes, which they attribute to increased nitrate formation at low temperatures.

N_a ranges from $\approx 1,500 \text{ cm}^{-3}$ to $\approx 4,050 \text{ cm}^{-3}$ across the fog cases, with a median value of $2,860 \text{ cm}^{-3}$ and 25th and 75th percentiles of $2,520$ and $3,590 \text{ cm}^{-3}$. These aerosol concentrations are fairly low compared to previous investigations in more populated or polluted areas. For example, Quan et al. (2011) found average N_a of $24,000 \text{ cm}^{-3}$ in the North China Plain, and Mazoyer et al. (2019) found that N_a varied between 2000 and $20,000 \text{ cm}^{-3}$ prior to fog events at the SIRTAs site near Paris, with the variation mainly depending on the prevailing wind direction. Aerosol loading and variation in the aerosol size distribution at the SGP site were investigated by Marinescu et al. (2019), who found a diurnal cycle in accumulation mode aerosols, with the highest concentrations occurring at night and being driven by nocturnal increases in nitrate and organic aerosol mass concentrations. The SGP site is rural and the surrounding area is primarily grassland and rangeland, so the lower N_a may reflect the reduced anthropogenic influence at this site compared to the sites used in previous studies; this is also supported by the relatively high κ values shown in Table 3 (as compared to values previously reported from suburban and urban areas).

Table 3 lists the minimum median dry activation diameter for each case. Values vary from 278–448 nm. However, the minimum $D_{\text{act}}^{\text{dry}}$ may occur for only a short period, as in the fog on 2019/08/04 shown in Figure 1. The change of $D_{\text{act}}^{\text{dry}}$ over time shown in Figure 1e illustrates that although the minimum $D_{\text{act}}^{\text{dry}}$ reaches 278 nm shortly before 10 UTC (corresponding to the time shown in Figure 1d), during the second half of the fog episode it is approximately 400 nm. Nucleation scavenging of larger particles during each event is also visible in Figures 5 and 6 shows an example sigmoid fit to the size-dependent fraction of particles scavenged for each fog event. During several of the cases, the strongest scavenging/lowest $D_{\text{act}}^{\text{dry}}$ occurs shortly after droplet activation begins at 10 m, and $D_{\text{act}}^{\text{dry}}$ then increases while the concentration of fog droplets decreases (see Figure 5). This cycle may be repeated multiple times (as on 2017/04/18, 2019/12/22) as the fog either dissipates and reforms or as the height of the fog increases and decreases below the AOS inlet height.

The range of $D_{\text{act}}^{\text{dry}}$ during each fog event can also be seen in Figure 7. At times, the $D_{\text{act}}^{\text{dry}}$ value is higher than 470 nm, which is the largest particle diameter recorded by the SMPS. This reflects times when the scavenging of even the largest particles is less than 50%. An example sigmoid fit when the scavenging of the largest particles is just above 50% can be seen in Figure 6 for 2018-12-01, when the corresponding $D_{\text{act}}^{\text{dry}}$ was 460 nm. In general, there is very little activation of particles with diameter <300 nm (Figure 5). This echoes results from previous investigations (Gilardoni et al., 2014; Hammer et al., 2014; Mazoyer et al., 2019) at sites with higher average aerosol loading and lower hygroscopicity. There are relatively few measurements available in the literature of the dry PSD evolution during a fog event at sites with lower aerosol concentrations for

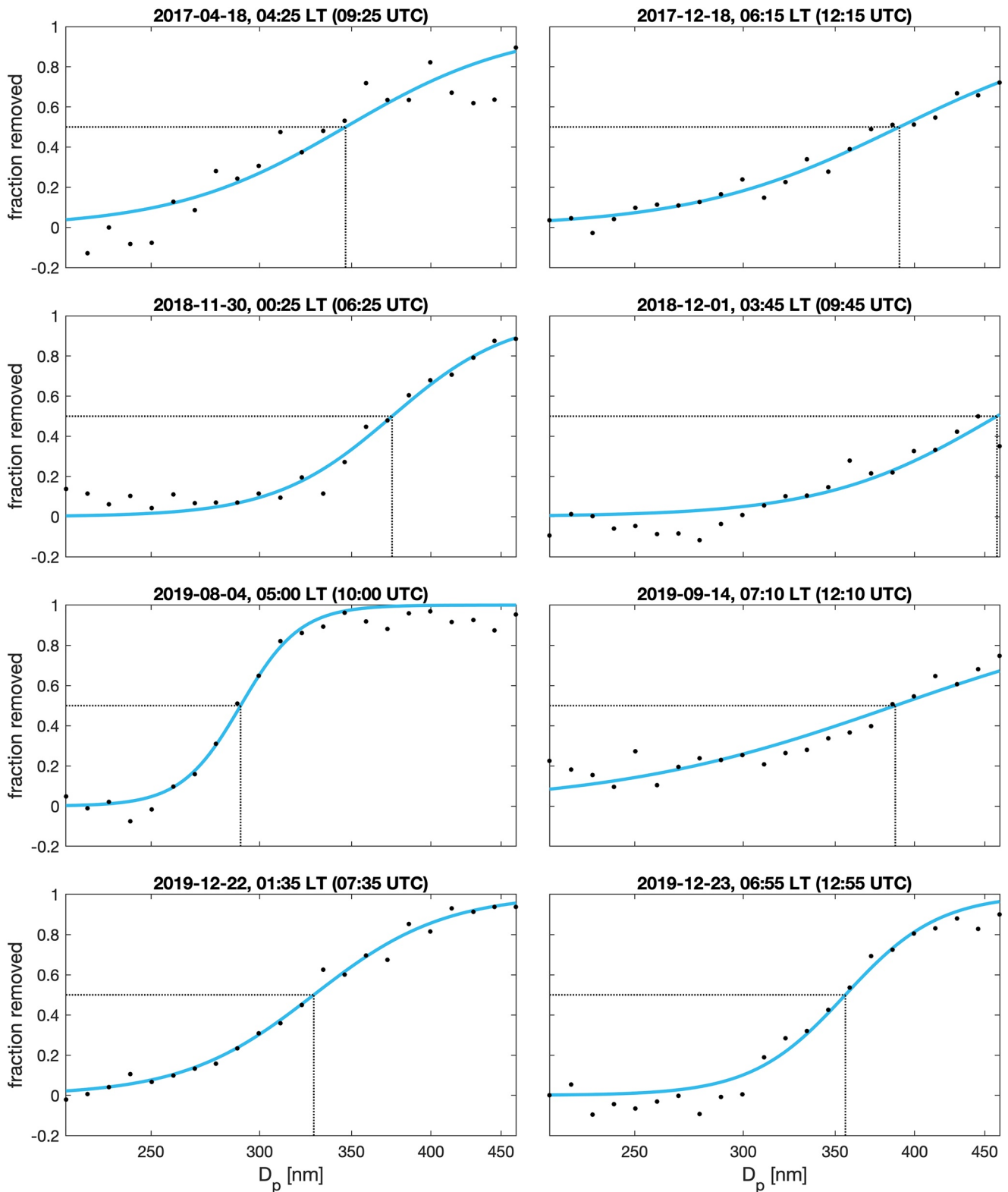


Figure 6. As for Figures 5 and 4, but showing the size-dependent particle scavenging from the scanning mobility particle sizer data and the corresponding sigmoid fit for a time period during each fog case. The black dashed line shows the 50% scavenging diameter (D_{act}^{dry}) from each fit.

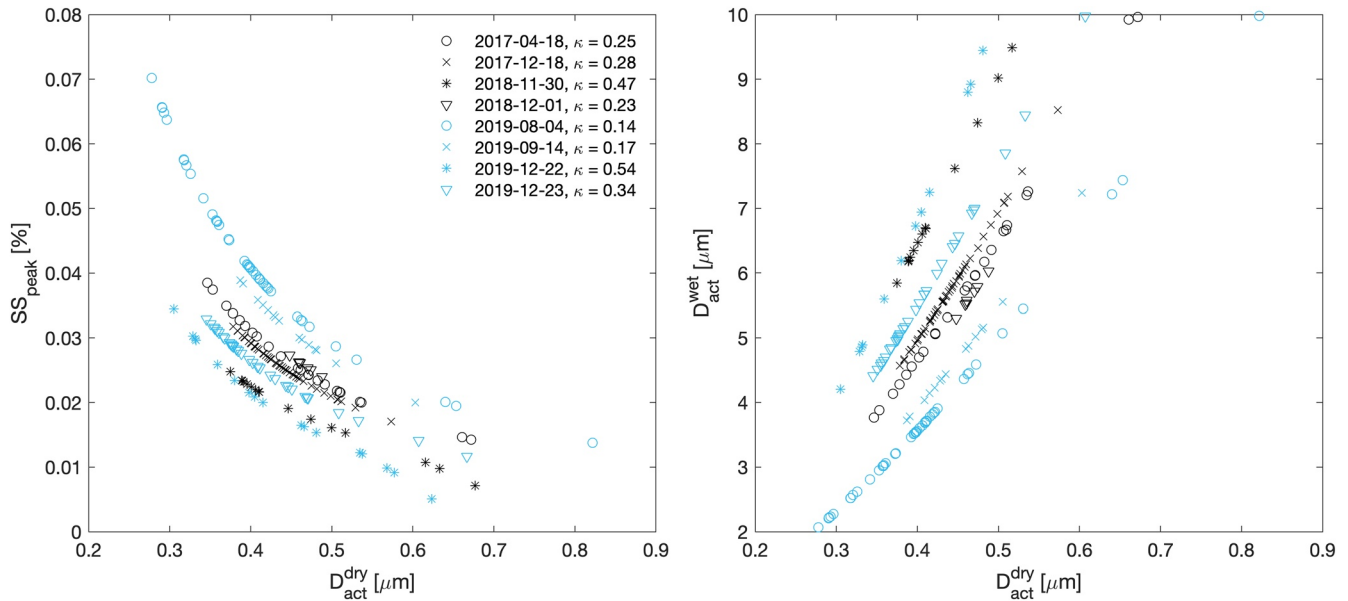


Figure 7. (a) The variation of SS_{peak} (calculated based on $\kappa_{SS=0.1\%}$) with D_{act}^{dry} for each fog event. The κ values in the legend are as in Figure 8; (b) The relation between D_{act}^{wet} and D_{act}^{dry} .

comparison, as most previous studies that have measured the aerosol PSD evolution during fog have done so at ambient humidity (e.g., Sasakawa et al., 2003).

Table 3 also shows the maximum value of SS_{peak} determined during each fog event. SS_{peak} varies depending on which value of κ is used in Equation 1, with higher κ giving lower SS_{peak} values for the same D_{act}^{dry} (see Figure 1h). When $\kappa_{SS=0.1\%}$ is used to calculate the peak supersaturation, SS_{peak} values range from 0.025%–0.04%, except for the fog event on 2019/08/04, when the low minimum activation diameter reached near the start of the fog (see Figure 1e) corresponds to the maximum SS_{peak} of 0.07%. While the SS_{peak} values shown in Table 3 represent the highest values seen during the fog, SS_{peak} varies over the course of the fog event as seen in Figure 1h. The range of derived SS_{peak} values for each case is illustrated in Figure 8. In general SS_{peak} is between 0.01%–0.04%, with the exception of the higher values seen on 2019/08/04. These SS_{peak} values are in line with critical supersaturation values found in previous observational campaigns (e.g., Hammer et al., 2014; Mazoyer et al., 2019; Shen et al., 2018) and numerical studies (e.g., Boutle et al., 2018).

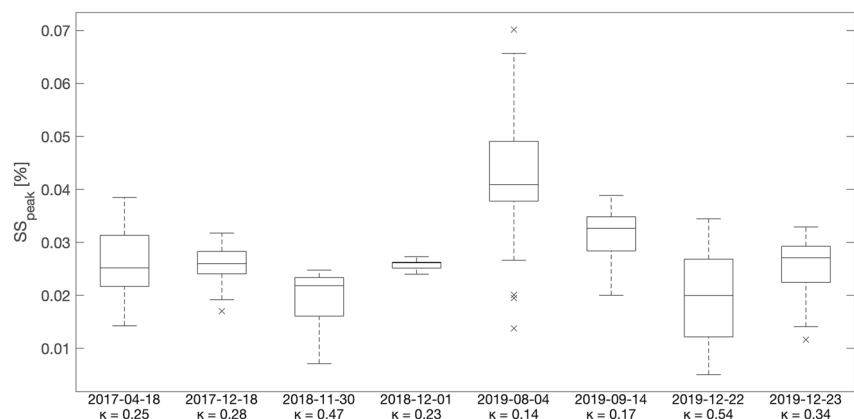


Figure 8. Boxplot of SS_{peak} (calculated based on $\kappa_{SS=0.1\%}$) for each of the fog events. $\kappa_{SS=0.1\%}$ for each case is listed. Since $\kappa_{SS=0.1\%}$ is not available on 2019/12/22, there SS_{peak} is calculated based on the size-dependent κ extrapolated to D_{act}^{dry} .

The variation of SS_{peak} with $D_{\text{act}}^{\text{dry}}$ during each fog event is shown in Figure 7a. The relationship between $D_{\text{act}}^{\text{dry}}$ and SS_{peak} is determined by κ , and it is clear that the $SS_{\text{peak}}-D_{\text{act}}^{\text{dry}}$ relation is clustered for fog events with similar values of $\kappa_{SS=0.1\%}$, such as 2017/04/18, 2017/12/18, and 2018/12/01. Figure 7a demonstrates that although $D_{\text{act}}^{\text{dry}}$ during a fog event varies monotonically with SS_{peak} , differences in κ between the cases can result in different $D_{\text{act}}^{\text{dry}}$ for the same SS_{peak} (and vice versa). For example, during the fog on 2019/12/22 when $\kappa_{400\text{nm}} = 0.54$, for an SS_{peak} of 0.03%, $D_{\text{act}}^{\text{dry}}$ is 330 nm. Conversely, on 2019/08/04, when κ is much lower ($\kappa_{SS=0.1\%} = 0.14$) for the same SS_{peak} of 0.03%, $D_{\text{act}}^{\text{dry}}$ is 496 nm. This lower κ value on 2019/08/04 is likely influenced by the increase in biogenic secondary organic aerosol at the SGP site during the summer (Parworth et al., 2015), although it is also similar to the typical κ seen in regions with high anthropogenic influences on the aerosols. Both cases reach similar minimum values of $D_{\text{act}}^{\text{dry}}$, but the difference in κ between the cases means that the supersaturation required to activate dry particles of a given size is much higher on 2019/08/04. It can be seen from Figure 7a that during the fog on 2019/08/04, a $D_{\text{act}}^{\text{dry}}$ of ≈ 300 nm corresponds to $SS_{\text{peak}} \approx 0.063\%$, while on 2019/12/22 when $\kappa_{SS=0.1\%}$ is much higher, $D_{\text{act}}^{\text{dry}} \approx 300$ nm equates to $SS_{\text{peak}} \approx 0.035\%$. As follows from κ -Köhler theory, for the same dry PSD, the higher the hygroscopicity of the accumulation and coarse mode aerosols is, the lower the supersaturation required to activate these particles and produce fog. So for the same thermodynamic setup and PSD, the particle hygroscopicity can be a decisive factor in the number of droplets that activate.

The method of determining the aerosol hygroscopicity using the SMPS and CCN counter data assumes that the aerosols are internally mixed (Mazoyer et al., 2019). If the larger dry particles are significantly externally mixed, then the relationship between κ and fog formation becomes more complex (Richter et al., 2021). For κ derived using the HT-DMA measurements, each monodisperse dry particle size produces a distribution of growth factors. The mean of the hydrated particle size distribution is taken as representative for that dry particle size and then used in Equation 1. Mahish and Collins (2017) examined the size-dependent growth factor distributions at the SGP site using HT-DMA data, where a threshold was applied to classify particles of a given size as internally or externally mixed based on the standard deviation of the growth factor distribution. Both a diel and seasonal cycle in a mixing state were observed, with internal mixtures more common during the summer and during the daytime. As fog is most common overnight and during late autumn to early spring, external mixing of particles may impact how hygroscopicity relates to size-dependent particle activation during fog events.

Figure 7b shows the wet activation diameters corresponding to the $D_{\text{act}}^{\text{dry}}$ values in Figure 7a. Similar to SS_{peak} , the ambient droplet size at activation ($D_{\text{act}}^{\text{wet}}$) for a given $D_{\text{act}}^{\text{dry}}$ will vary depending on κ , as seen in Figure 7b. For less hygroscopic particles with lower κ , the wet activation diameter is decreased compared to days with higher κ . On 2019/08/04 with $\kappa = 0.14$, a $D_{\text{act}}^{\text{dry}}$ of 400 nm corresponds to a wet activation diameter of 3.5 μm , whereas on 2019/12/22 when $\kappa_{400\text{nm}} = 0.54$ this is increased to 6.8 μm . Hammer et al. (2014) found the median $D_{\text{act}}^{\text{wet}}$ to range from 1 to 5 μm with a median value of 2.6 μm during the ParisFog campaign. We find slightly higher $D_{\text{act}}^{\text{wet}}$ values at the SGP site (see Figure 7) which is to be expected due to the higher average κ compared to the ParisFog site. The high values of $D_{\text{act}}^{\text{wet}}$ highlight the strong contribution that hydrated but unactivated particles make during radiative fog events. Figure 7 indicates that with the exception of the fog event on 2019/08/04, all particles with diameters below 3.5 μm in the fog are unactivated. These hydrated but unactivated particles still cause extinction of visible radiation and Elias et al. (2009) demonstrated using calculations based on Mie theory that unactivated particles were responsible for $20 \pm 10\%$ of the visibility reduction in fog episodes during the ParisFog field campaign. At sites where κ is higher and thus $D_{\text{act}}^{\text{wet}}$ is higher for the same supersaturation, the contribution of unactivated particles to visibility reduction may be more pronounced.

Short periods of higher supersaturation may occur that are not reflected in SS_{peak} due to the 5-min update time of the SMPS measurements. Gerber (1991) presents supersaturation values in fog measured at high temporal resolution using a saturation hygrometer, finding short-lived supersaturations reaching as high as 0.3%. Additionally, if the timescale of the turbulent fluctuations in supersaturation is shorter than the timescale required for the droplets to adjust to the increased supersaturation, then the droplet activation state will not accurately reflect the ambient supersaturation even for high temporal resolution measurements (Prabhakaran et al., 2020; Richter et al., 2021).

In regions with high aerosol loading, the high aerosol concentration can lead to competition between a large number of activated droplets or hydrated but unactivated particles. This effect keeps the particle effective radius low, increasing the fog optical depth and strengthening the radiative effect of the fog (Quan et al., 2011; Shen et al., 2018). By decreasing the droplet effective radius, the removal of droplets via sedimentation is also slowed if the aerosol concentration is high. The competition for water vapor between droplets can also suppress the supersaturation when aerosol concentration is high, as demonstrated numerically by Poku et al. (2021). On the other hand, at more pristine sites particle scavenging may be enhanced by higher effective peak supersaturations (Collett et al., 2008). We do not see a strong relationship between N_a and SS_{peak} across the cases included in our analysis (a linear model fit gives R^2 of 0.08). This is perhaps not surprising given the range of κ across the cases: Table 3 shows that the fog events on 2019/08/04 and 2019/12/23 had very similar N_a of 2,830 and 2,820 cm^{-3} respectively, but the differences in κ (0.14 vs. 0.34) resulted in maximum peak supersaturations of 0.070% and 0.033%. It may also be there is insufficient variation in N_a across the cases (1,510–4,050 cm^{-3}) for this effect to be apparent in our data. Poku et al. (2021) tested aerosol activation schemes using PSDs representing marine, clean continental, and urban conditions (based on Whitby, 1978), and while strong differences were seen between the resulting fog activation and development, the accumulation mode aerosol concentration varied from 60–32,000 cm^{-3} across the three PSDs. Additional measurements of aerosol scavenging in fog from locations with a wide range of background aerosol concentrations would be helpful to further examine this effect and facilitate comparisons with model output.

The method that we are using requires the assumption that the background aerosol content (in terms of concentration and particle size distribution) does not change substantially during the fog event, say, due to horizontal advection from an external source. We characterize the aerosol content in the hour prior to the fog event and use that PSD as a baseline against which to assess nucleation scavenging. This method was followed by Mazoyer et al. (2019), and similarly Noone et al. (1992) characterized the aerosol content over a 15-min period 1 hr before fog started and used this PSD to evaluate aerosol scavenging in fog in the Po Valley in Italy. Changes in the aerosol loading over the course of the fog events should be reduced by the low wind speed typical in radiation fog, although changes to the PSD due to small-scale effects (e.g., localized drainage flows or local transport) may occur. Even at the low wind speeds that occur during radiation fog, over the course of several hours this could lead to transport over tens of kilometers. For example, the fog event on 2017/04/18 lasted 5 hr with a mean wind speed of 2.9 m s^{-1} , which corresponds to the air mass covering a distance of 52 km. Some changes in the dry PSD when comparing prior to fog onset with after the fog has ended can be seen in Figure 5, for example the 350–400 nm aerosol concentration is higher after the fog has ended than before it began on 2019/12/23. Noone et al. (1992) notes that the effects of nucleation scavenging will often be confounded by changes in the aerosol PSD over the course of a fog event. However, the strongest scavenging is often seen to occur shortly after fog onset at the inlet height (Figures 4 and 5), when less time has passed since the dry PSD was characterized. As such, the effect of local transport on the minimum activation diameters shown in Table 3 should not be significant, although this issue should be kept in mind when examining time series during longer fog events when stronger changes to the background PSD may have occurred. This reasoning is also why we do not include cases of stratus lowering fog in the analysis, as the particles which serve as CCN in those cases may originate at higher altitudes and so their relation to the surface aerosol characteristics is uncertain.

One caveat of the method used here is the potential for some fog droplet residuals to be included in the SMPS data. Should fog droplet residuals be present in the dry PSD during the fog, this would artificially increase D_{act}^{dry} compared to the true value, which would lead to underestimation of SS_{peak} (for a given κ). However, given the almost total removal of large particles in the dry PSD at the start of the fog event as shown in Figures 1c and 1d, combined with the reduced transmission efficiency for fog droplets of diameter $\approx 10 \mu\text{m}$ reported by Andrews et al. (2019), we expect that few fog droplet residuals are present in the dry PSD. As such we consider that the effect of fog droplet residuals on the retrieved activation properties should be minor.

The method presented here also does not account for two other processes that may affect the derived supersaturation. The first of these is the removal of aerosols via impaction scavenging by fog droplets. Although nucleation scavenging is generally understood to be the dominant scavenging process in fog due to the small size and low volume fraction of the fog droplets limiting their swept area, impaction scavenging can

also act as a source of aerosol removal. Impaction scavenging would remove aerosols from the distribution, potentially leading to a high bias in SS_{peak} , although we expect this effect to play a minor role compared to the other processes described here due to the relatively low number concentration of fog droplets. Further evidence that impaction scavenging is not a major source of aerosol removal in the cases examined here is that the total aerosol concentration does not strongly decrease during each fog event. The second process is the gravitational settling of hydrated but unactivated aerosols. Figure 7 shows the wet activation diameter for each of the cases, which ranges from 2 μm up to greater than 5 μm , meaning that hydrated aerosols can reach sizes of up to 5 μm while remaining unactivated. The 5- μm hydrated aerosols will have fall speeds of around 0.75 mm s^{-1} , or 2.7 m hr^{-1} . For a fog height of 10 m (the height of the AOS inlet), these hydrated particles would take around 3.7 h to reach the ground (neglecting the effects of turbulence) and be removed via wet deposition. As the hydrated aerosols fall below the inlet height, they will be effectively removed from the distribution. This effect would introduce a low bias to $D_{\text{dry}}^{\text{act}}$, potentially resulting in a high bias in SS_{peak} . Similarly, uncertainty in the inlet transmission efficiency for particles with diameter $\geq 4 \mu\text{m}$ could mean that some large hydrated but unactivated aerosols are also removed prior to entering the SMPS. The loss of these particles in the tubing or drying process would be attributed to nucleation scavenging, artificially lowering $D_{\text{dry}}^{\text{act}}$ and potentially creating a high bias in SS_{peak} .

The analysis is also limited by the maximum dry particle size measured by the SMPS. The activation of particles with dry diameters above 470 nm is not included when deriving κ using the CCN counter and SMPS measurements. If there is a significant concentration of particles with dry diameters above 470 nm, then D_{crit} in Equation 3 will be artificially decreased, leading to an overestimation of the true value of κ . However the SGP site generally has very low concentrations of particles with dry size above ≈ 500 nm (Marinescu et al., 2019), and so we expect that large dry particles not captured by the SMPS will not significantly alter the supersaturation values presented here.

Although we demonstrate two methods of deriving κ in Figure 2, some previous studies have revealed discrepancies between the hygroscopicity when derived using measurements at supersaturated and subsaturated conditions (see for example Irwin et al., 2010; Petters et al., 2009; Wex et al., 2009). A meta-analysis of particle water uptake studies comparing hygroscopicity at supersaturated and subsaturated conditions was conducted by Whitehead et al. (2014), finding that at most sites the agreement was within the measurement variability, although at some sites the agreement was poor, especially when the derived κ was used to evaluate CCN activity at low supersaturations. Both methods of deriving the supersaturation have been applied in recent studies of supersaturation in fog: Mazoyer et al. (2019) used the SMPS and CCN counter method for deriving κ , where the measurements are taken at supersaturated conditions, while Shen et al. (2018) used the HT-DMA method, where the particle hygroscopicity is derived based on the size-resolved growth factor at subsaturated conditions. For the eight cases shown in Table 3, κ from the SMPS and CCN method is presented for seven of the cases and κ from the HT-DMA data is shown for four cases (three of these cases overlap). The supersaturation values and wet activation diameters shown in Figures 7 and 8 are calculated using the supersaturated measurements (from the SMPS and CCN data) for all cases for which it is available; on 2019/12/22 κ derived from subsaturated conditions is shown as $\kappa_{SS=0.1\%}$ was unavailable. Due to the uncertainties outlined by Irwin et al. (2010), we suggest that if κ derived from SMPS and CCN measurements is available, this should be used over κ derived from the subsaturated growth factor. An additional uncertainty that arises when using the HT-DMA data relates to the extrapolation of κ beyond the largest dry particle size measured by the HT-DMA; there exists an upper limit to κ for large dry particle sizes, so extrapolation may lead to overestimation of κ for larger accumulation mode particles. Despite ongoing research and discussion on the causes of the discrepancies in κ depending on how it is calculated, it is interesting that the hygroscopicity, critical diameter, and ambient supersaturation across the three overlapping fog events using both methods shown in Table 3 are quite similar and in most cases result in derived supersaturations that are within the margins of uncertainty, suggesting that these issues were not as important during our study periods.

In addition, the aerosol mixing state was not determined for the cases presented here. Use of the SMPS and CCN data to derive the hygroscopicity relies on the assumption that the aerosols are internally mixed. Mahish et al. (2018) tested the impact of several assumptions about mixing state on the predicted concentration of CCN at the ARM SGP site, finding that the assumption of internally mixed aerosols with size-dependent

κ (as used here) resulted in the best agreement with the measured CCN concentrations. As such, we believe it is reasonable to assume that the aerosols are internally mixed and that κ increases with particle size. However, if there is significant external mixing at particle diameters ≥ 300 nm, the relationship between κ and SS_{peak} becomes complex and cannot be fully captured by the methods used in this study.

4. Conclusions

In this paper, we examine aerosol activation during several radiative fog events in north-central Oklahoma, USA. We derive the particle hygroscopicity (κ) for each case based on two independent techniques: size-dependent particle growth factors and matching the dry particle size distribution with the measured CCN concentration at different supersaturations. Changes in the dry particle size distribution during the fog compared to the hour before the fog are used to evaluate the median dry activation diameter. κ -Köhler theory is applied to calculate the critical supersaturation required to activate particles with that dry diameter and κ , as well as the wet activation diameter.

Despite the importance of supersaturation in fog formation, measuring supersaturation in fog has long been a difficult task due to the high accuracy required to capture the low ambient supersaturations typical in radiation fog (e.g., Gerber, 1991). The extension of the well-known Köhler theory (Köhler, 1936) to account for hygroscopicity by Petters and Kreidenweis (2007) provided a new theoretical basis for researchers to analyze supersaturation in fog. If the hygroscopicity of the particles is known or can be calculated or assumed, then κ -Köhler theory allows the critical supersaturation to be calculated based on the particle activation diameter or vice versa. This method has been applied to calculate the peak effective supersaturation in fog during the ParisFog campaign (Hammer et al., 2014; Mazoyer et al., 2019) and the HaChi (Haze in China) experiment (Shen et al., 2018).

Although the SGP site has much lower average aerosol loading than the other sites where the method described here has been implemented, we find very similar effective peak supersaturations to other sites with higher aerosol loading (Hammer et al., 2014; Mazoyer et al., 2019; Shen et al., 2018). During seven of the eight fog events, SS_{peak} was below 0.04%. The fog event on 2019/08/04 showed higher SS_{peak} values of 0.04%–0.07% during the first 2 hr, and this event has the highest concentration of activated droplets of any of the fog episodes. The high concentration of activated droplets contributed to this case having the lowest median visibility out of any of the events. While radiative fog most often occurs during the autumn and winter when night length is longest and temperatures are low, two of the fog cases shown here occurred during summer and early autumn when temperatures were $\approx 20^\circ\text{C}$, but the water vapor mixing ratio was sufficiently high for saturation to occur.

The fraction of particles removed via nucleation scavenging increases monotonically with increasing particle size, as expected in κ -Köhler theory. This effect can be further enhanced if the particle hygroscopicity increases with particle size. In general, we find very little activation of particles with dry diameters below 300 nm, as in Noone et al. (1992). The median wet activation diameter varies strongly both between cases (as also noted by Hammer et al., 2014) and also over time during each case with values from 2 μm to more than 7 μm . This highlights the difficulties in choosing a threshold diameter to delineate between hydrated particles and activated droplets, as the appropriate threshold will change over time based on the dry particle size distribution and particle hygroscopicity. This provides an important consideration when planning an inlet cutoff size for separating fog droplets (and their residuals) from hydrated interstitial particles during field campaigns.

Data Availability Statement

Data for this study are available at: Atmospheric Radiation Measurement (ARM) user facility (1993); Atmospheric Radiation Measurement (ARM) user facility (2017a, 2017b); and Atmospheric Radiation Measurement (ARM) user facility (2016a, 2016b, 2016c).

Acknowledgments

This research was funded by the Office of Naval Research Award N00014-18-1-2472 entitled Toward Improving Coastal Fog Prediction (C-FOG). Data were obtained from the Atmospheric Radiation Measurement (ARM) Climate Research Facility, a US Department of Energy Office of Science user facility sponsored by the Office of Biological and Environmental Research. We thank Dr. Chongai Kuang for helpful discussions about the instrument setup in the ARM SGP aerosol observing system, and Dr. Gourihar Kulkarni for providing details on the calculation of κ in the ARM CCNSMP-SKAPPA value added product.

References

Andrews, E., Sheridan, P. J., Ogren, J. A., Hageman, D., Jefferson, A., Wendell, J., et al. (2019). Overview of the NOAA/ESRL federated aerosol network. *Bulletin of the American Meteorological Society*, 100(1), 123–135. <https://doi.org/10.1175/BAMS-D-17-0175.1>

Atmospheric Radiation Measurement (ARM) user facility. (1993). Surface Meteorological Instrumentation (MET). In J. Kyrouac, M. Ritsche, N. Hickmon, & D. Holdridge (Eds.), 2017/04/18 to 2019/12/23, *Southern Great Plains (SGP) Lamont, OK (extended and co-located with C1) (E13)*. ARM Data Center. <https://doi.org/10.5439/1025220>

Atmospheric Radiation Measurement (ARM) user facility. (2016a). Aerodynamic particle sizer (AOSAPS). In A. Koontz & A. Sedlacek (Eds.), 2017/04/18 to 2019/12/23, *Southern Great Plains (SGP) Lamont, OK (extended and co-located with C1) (E13)*. ARM Data Center. <https://doi.org/10.5439/1248461>

Atmospheric Radiation Measurement (ARM) user facility. (2016b). Condensation particle counter (AOSPCPF). In C. Kuang, J. Wang, C. Salwen, M. Boyer, & A. Singh (Eds.), 2017/04/18 to 2019/12/23, *Southern Great Plains (SGP) Lamont, OK (extended and co-located with C1) (E13)*. ARM Data Center. <https://doi.org/10.5439/1046184>

Atmospheric Radiation Measurement (ARM) user facility. (2016c). Scanning mobility particle sizer (AOSNANOSMPS). In C. Kuang, & B. Ermold (Eds.), 2017/04/18 to 2019/12/23, *Southern Great Plains (SGP) Lamont, OK (extended and co-located with C1) (E13)*. ARM Data Center. <https://doi.org/10.5439/1635016>

Atmospheric Radiation Measurement (ARM) user facility. (2017a). CCN counter and SMPS derived hygroscopicity parameter kappa (AOSCCNSMPSKAPPA). In G. Kulkarni, & M. Levin (Eds.), 2017/04/18 to 2019/12/23, *Southern Great Plains (SGP) Lamont, OK (extended and co-located with C1) (E13)*. ARM Data Center. <https://doi.org/10.5439/1729907>

Atmospheric Radiation Measurement (ARM) user facility. (2017b). Humidified Tandem Differential Mobility Analyzer (AOSHTDMA). In J. Uin & E. Cromwel (Eds.), 2017/04/18 to 2019/12/23, *Southern Great Plains (SGP) Lamont, OK (extended and co-located with C1) (E13)*. ARM Data Center. <https://doi.org/10.5439/1095581>

Bott, A. (1991). On the influence of the physico-chemical properties of aerosols on the life cycle of radiation fogs. *Boundary-Layer Meteorology*, 56(1–2), 1–31. <https://doi.org/10.1007/BF00119960>

Boutle, L., Price, J., Kudzsotsa, I., Kokkola, H., & Romakkaniemi, S. (2018). Aerosol–fog interaction and the transition to well-mixed radiation fog. *Atmospheric Chemistry and Physics*, 18(11), 7827–7840. <https://doi.org/10.5194/acp-18-7827-2018>

Bullard, R., Kuang, C., Uin, J., Smith, S., & Springston, S. (2017). *Aerosol inlet characterization experiment report*. Tech. Rep. No. DOE/SC-ARM-TR-191. <https://doi.org/10.2172/1355300>

Collett, J. L., Herckes, P., Youngster, S., & Lee, T. (2008). Processing of atmospheric organic matter by California radiation fogs. *Atmospheric Research*, 87(3–4), 232–241. <https://doi.org/10.1016/j.atmosres.2007.11.005>

Elias, T., Haeffelin, M., Drobinski, P., Gomes, L., Rangognio, J., Bergot, T., & Colomb, M. (2009). Particulate contribution to extinction of visible radiation: Pollution, haze, and fog. *Atmospheric Research*, 92(4), 443–454. <https://doi.org/10.1016/j.atmosres.2009.01.006>

Fitzjarrald, D. R., & Lala, G. G. (1989). Hudson Valley fog environments. *Journal of Applied Meteorology*, 28(12), 1303–1328. [https://doi.org/10.1175/1520-0450\(1989\)028<1303:hvfe>2.0.co;2](https://doi.org/10.1175/1520-0450(1989)028<1303:hvfe>2.0.co;2)

Gerber, H. (1991). Supersaturation and droplet spectral evolution in fog. *Journal of the Atmospheric Sciences*, 48(24), 2569–2588. [https://doi.org/10.1175/1520-0469\(1991\)048<2569:sadsei>2.0.co;2](https://doi.org/10.1175/1520-0469(1991)048<2569:sadsei>2.0.co;2)

Ghude, S. D., Bhat, G. S., Prabhakaran, T., Jenamani, R. K., Chate, D. M., Safai, P. D., & Rajeevan, M. (2017). Winter fog experiment over the Indo-Gangetic plains of India. *Current Science*, 112(4), 767–784. <https://doi.org/10.18520/cs/v112/i04/767-784>

Gilardoni, S., Massoli, P., Giulianelli, L., Rinaldi, M., Paglione, M., Pollini, F., & Fuzzi, S. (2014). Fog scavenging of organic and inorganic aerosol in the Po Valley. *Atmospheric Chemistry and Physics*, 14(13), 6967–6981. <https://doi.org/10.5194/acp-14-6967-2014>

Gray, E., Gilardoni, S., Baldocchi, D., McDonald, B. C., Facchini, M. C., & Goldstein, A. H. (2019). Impact of air pollution controls on radiation fog Frequency in the Central Valley of California. *Journal of Geophysical Research: Atmospheres*, 1–17. <https://doi.org/10.1029/2018JD029419>

Gultepe, I., & Isaac, G. A. (1999). Scale effects on averaging of cloud droplet and aerosol number concentrations: Observations and models. *Journal of Climate*, 12(5 1), 1268–1279. [https://doi.org/10.1175/1520-0442\(1999\)012<1268:seoac>2.0.co;2](https://doi.org/10.1175/1520-0442(1999)012<1268:seoac>2.0.co;2)

Gultepe, I., Tardif, R., Michaelides, S. C., Cermak, J., Bott, A., Bendix, J., & Cober, S. G. (2007). Fog research: A review of past achievements and future perspectives. *Pure and Applied Geophysics*, 164(6–7), 1121–1159. <https://doi.org/10.1007/s00024-007-0211-x>

Haeffelin, M., Bergot, T., Elias, T., Tardif, R., Carrer, D., Chazette, P., & Zhang, X. (2010). PARISFOG: Shedding new light on fog physical processes. *Bulletin of the American Meteorological Society*, 91(6), 767–783. <https://doi.org/10.1175/2009BAMS2671.1>

Hammer, E., Gysel, M., Roberts, G. C., Elias, T., Hofer, J., Hoyle, C. R., & Weingartner, E. (2014). Size-dependent particle activation properties in fog during the ParisFog 2012/13 field campaign. *Atmospheric Chemistry and Physics*, 14(19), 10517–10533. <https://doi.org/10.5194/acp-14-10517-2014>

Hudson, J. G. (1980). Relationship between fog condensation nuclei and fog microstructure. *Journal of the Atmospheric Sciences*, 37(8), 1854–1867. [https://doi.org/10.1175/1520-0469\(1980\)037<1854:rbcna>2.0.co;2](https://doi.org/10.1175/1520-0469(1980)037<1854:rbcna>2.0.co;2)

Irwin, M., Good, N., Crosier, J., Choulaton, T. W., & McFiggans, G. (2010). Reconciliation of measurements of hygroscopic growth and critical supersaturation of aerosol particles in central Germany. *Atmospheric Chemistry and Physics*, 10(23), 11737–11752. <https://doi.org/10.5194/acp-10-11737-2010>

Izett, J. G., Schilperoort, B., Coenders-Gerrits, M., Baas, P., Bosveld, F. C., & van de Wiel, B. J. H. (2019). Missed Fog? *Boundary-Layer Meteorology*, 173, 289–309. <https://doi.org/10.1007/s10546-019-00462-3>

Jefferson, A., Hageman, D., Morrow, H., Mei, F., & Watson, T. (2017). Seven years of aerosol scattering hygroscopic growth measurements from SGP: Factors influencing water uptake. *Journal of Geophysical Research: Atmospheres*, 122(17), 9451–9466. <https://doi.org/10.1002/2017JD026804>

Jia, X., Quan, J., Zheng, Z., Liu, X., Liu, Q., He, H., & Liu, Y. (2019). Impacts of anthropogenic aerosols on fog in North China Plain. *Journal of Geophysical Research: Atmospheres*, 124(1), 252–265. <https://doi.org/10.1029/2018JD029437>

Köhler, H. (1936). The nucleus in and the growth of hygroscopic droplets. *Transactions of the Faraday Society*, 32, 1152–1161. <https://doi.org/10.1039/TF9363201152>

Kokkola, H., Romakkaniemi, S., & Laaksonen, A. (2003). On the formation of radiation fogs under heavily polluted conditions. *Atmospheric Chemistry and Physics*, 3(3), 581–589. <https://doi.org/10.5194/acp-3-581-2003>

Kulkarni, G. R., Levin, M. S., & Shilling, J. E. (2021). *Cloud condensation nuclei hygroscopicity value-added product report (Tech. Rep. No. DOE/SC-ARM-TR-272)*. US Department of Energy.

Lance, S., Medina, J., Smith, J., & Nenes, A. (2006). Mapping the operation of the DMT continuous flow CCN counter. *Aerosol Science and Technology*, 40(4), 242–254. <https://doi.org/10.1080/02786820500543290>

- Maalick, Z., Kühn, T., Korhonen, H., Kokkola, H., Laaksonen, A., & Romakkaniemi, S. (2016). Effect of aerosol concentration and absorbing aerosol on the radiation fog life cycle. *Atmospheric Environment*, *133*, 26–33. <https://doi.org/10.1016/j.atmosenv.2016.03.018>
- Mahish, M., & Collins, D. (2017). Analysis of a multi-year record of size-resolved hygroscopicity measurements from a rural site in the U.S. *Aerosol and Air Quality Research*, *17*(6), 1389–1400. <https://doi.org/10.4209/aaqr.2016.10.0443>
- Mahish, M., Jefferson, A., & Collins, D. R. (2018). Influence of common assumptions regarding aerosol composition and mixing state on predicted CCN concentration. *Atmosphere*, *9*(2). <https://doi.org/10.3390/atmos9020054>
- Marinescu, P. J., Levin, E. J., Collins, D., Kreidenweis, S. M., & Van Den Heever, S. C. (2019). Quantifying aerosol size distributions and their temporal variability in the Southern Great Plains, USA. *Atmospheric Chemistry and Physics*, *19*(18), 11985–12006. <https://doi.org/10.5194/acp-19-11985-2019>
- Mazoyer, M., Burnet, F., Denjean, C., Roberts, G. C., Dupont, J.-C., & Elias, T. (2019). Experimental study of the aerosol impact on fog microphysics at the instrumented site for atmospheric remote sensing. *Atmospheric Chemistry and Physics*, *19*, 4323–4344. <https://doi.org/10.5194/acp-19-4323-2019>
- Mülmenstädt, J., & Feingold, G. (2018). The radiative forcing of aerosol–cloud interactions in liquid clouds: State of the field. *Current Climate Change Reports*, *4*, 23–40. <https://doi.org/10.1007/s40641-018-0089-y>
- Noone, K. J., Ogren, J. A., Hallberg, A., Heintzenberg, J., Strom, J., Hansson, H.-C., & Berner, A. (1992). Changes in aerosol size- and phase distributions due to physical and chemical processes in fog. *Tellus*, *44B*, 489–504. <https://doi.org/10.3402/tellusb.v44i5.15563>
- Parworth, C., Fast, J., Mei, F., Shippert, T., Sivaraman, C., Tilp, A., & Zhang, Q. (2015). Long-term measurements of submicrometer aerosol chemistry at the Southern Great Plains (SGP) using an Aerosol Chemical Speciation Monitor (ACSM). *Atmospheric Environment*, *106*, 43–55. <https://doi.org/10.1016/j.atmosenv.2015.01.060>
- Petters, M. D., & Kreidenweis, S. M. (2007). A single parameter representation of hygroscopic growth and cloud condensation nucleus activity. *Atmospheric Chemistry and Physics*, *7*(8), 1961–1971. <https://doi.org/10.5194/acp-7-1961-2007>
- Petters, M. D., Wex, H., Carrico, C. M., Hallbauer, E., Massling, A., McMeeking, G. R., & Stratmann, F. (2009). Towards closing the gap between hygroscopic growth and activation for secondary organic aerosol-Part 2: Theoretical approaches. *Atmospheric Chemistry and Physics*, *9*(12), 3999–4009. <https://doi.org/10.5194/acp-9-3999-2009>
- Phillips, B. N., Royalty, T. M., Dawson, K. W., Reed, R., Petters, M. D., & Meskhidze, N. (2018). Hygroscopicity- and Size-Resolved Measurements of Submicron Aerosol on the East Coast of the United States. *Journal of Geophysical Research: Atmospheres*, *123*(3), 1826–1839. <https://doi.org/10.1002/2017JD027702>
- Poku, C., Ross, A., Hill, A., Blyth, A., & Shipway, B. (2021). Is a more physical representation of aerosol activation needed for simulations of fog? *Atmospheric Chemistry and Physics*, *21*, 7271–7292. <https://doi.org/10.5194/acp-21-7271-2021>
- Poku, C., Ross, A. N., Blyth, A. M., Hill, A. A., & Price, J. D. (2019). How important are aerosol–fog interactions for the successful modelling of nocturnal radiation fog? *Weather*, *74*(7), 237–243. <https://doi.org/10.1002/wea.3503>
- Prabhakaran, P., Shawon, A. S. M., Kinney, G., Thomas, S., Cantrell, W., & Shaw, R. A. (2020). The role of turbulent fluctuations in aerosol activation and cloud formation. *Proceedings of the National Academy of Sciences of the United States of America*, *117*(29), 16831–16838. <https://doi.org/10.1073/pnas.2006426117>
- Price, J., Lane, S., Boutle, I., Smith, D. K. E., Bergot, T., Lac, C., & Clark, R. (2018). LANFEX: A field and modeling study to improve our understanding and forecasting of radiation fog. *Bulletin of the American Meteorological Society*, *99*(10), 2061–2077. <https://doi.org/10.1175/BAMS-D-16-0299.1>
- Quan, J., Liu, Y., Jia, X., Liu, L., Dou, Y., Xin, J., & Seinfeld, J. H. (2021). Anthropogenic aerosols prolong fog lifetime in China. *Environmental Research Letters*, *16*(4). <https://doi.org/10.1088/1748-9326/abef32>
- Quan, J., Zhang, Q., He, H., Liu, J., Huang, M., & Jin, H. (2011). Analysis of the formation of fog and haze in North China Plain (NCP). *Atmospheric Chemistry and Physics*, *11*(15), 8205–8214. <https://doi.org/10.5194/acp-11-8205-2011>
- Reutter, P., Su, H., Trentmann, J., Simmel, M., Rose, D., Gunthe, S. S., & Pöschl, U. (2009). Aerosol- and updraft-limited regimes of cloud droplet formation: Influence of particle number, size and hygroscopicity on the activation of cloud condensation nuclei (CCN). *Atmospheric Chemistry and Physics*, *9*(18), 7067–7080. <https://doi.org/10.5194/acp-9-7067-2009>
- Richter, D. H., MacMillan, T., & Wainwright, C. (2021). A Lagrangian cloud model for the study of marine fog. *Boundary-layer meteorology*. <https://doi.org/10.1007/s10546-020-00595-w>
- Sasakawa, M., Ooki, A., & Uematsu, M. (2003). Aerosol size distribution during sea fog and its scavenge process of chemical substances over the northwestern North Pacific. *Journal of Geophysical Research*, *108*(3), 1–9. <https://doi.org/10.1029/2002JD002329>
- Shen, C., Zhao, C., Ma, N., Tao, J., Zhao, G., Yu, Y., & Kuang, Y. (2018). Method to estimate water vapor supersaturation in the ambient activation process using aerosol and droplet measurement data. *Journal of Geophysical Research: Atmospheres*, *123*(18), 606–610. <https://doi.org/10.1029/2018JD028315>
- Sisterton, D. L., Pepler, R. A., Cress, T. S., Lamb, P. J., & Turner, D. D. (2016). The ARM southern great plains (SGP) site. *Meteorological Monographs*, *57*, 6.1–6.14. <https://doi.org/10.1175/AMSMONOGRAPH5-D-16-0004.1>
- Stolaki, S., Haefelin, M., Lac, C., Dupont, J.-C., Elias, T., & Masson, V. (2015). Influence of aerosols on the life cycle of a radiation fog event. A numerical and observational study. *Atmospheric Research*, *151*, 146–161. <https://doi.org/10.1016/j.atmosres.2014.04.013>
- Tanaka, H., Honma, S., Nishi, M., Igarashi, T., Teramoto, S., Nishio, F., & Abe, S. (1998). Acid fog and hospital visits for asthma: An epidemiological study. *European Respiratory Journal*, *11*(6), 1301–1306. <https://doi.org/10.1183/09031936.98.11061301>
- Turner, D. D., & Long, C. (2004). Direct aerosol forcing in the infrared at the SGP site? In *Presented at the Proceedings of the 14th Arm Science Team Meeting* (pp. 22–26).
- Turner, D. D., Vogelmann, A. M., Austin, R. T., Barnard, J. C., Cady-Pereira, K., Chiu, J. C., & Wiscombe, W. (2007). Thin liquid water clouds: Their importance and our challenge. *Bulletin of the American Meteorological Society*, *88*(2), 177–190. <https://doi.org/10.1175/BAMS-88-2-177>
- Uin, J. (2016). *Cloud condensation nuclei particle counter (CCN) instrument Handbook (Tech. Rep.)*. ARM Tech. Rep. DOE/SC-ARM-TR-168.
- Uin, J., Aiken, A. C., Dubey, M. K., Kuang, C., Pekour, M., Salwen, C., & Springston, S. R. (2019). Atmospheric radiation measurement (ARM) aerosol observing systems (AOS) for surface-based in situ atmospheric aerosol and trace gas measurements. *Journal of Atmospheric and Oceanic Technology*, *36*(12), 2429–2447. <https://doi.org/10.1175/JTECH-D-19-0077.1>
- Van Oldenborgh, G. J., Yiou, P., & Vautard, R. (2010). On the roles of circulation and aerosols in the decline of mist and dense fog in Europe over the last 30 years. *Atmospheric Chemistry and Physics*, *10*(10), 4597–4609. <https://doi.org/10.5194/acp-10-4597-2010>
- Wex, H., Petters, M. D., Carrico, C. M., Hallbauer, E., Massling, A., McMeeking, G. R., & Stratmann, F. (2009). Towards closing the gap between hygroscopic growth and activation for secondary organic aerosol: Part 1-Evidence from measurements. *Atmospheric Chemistry and Physics*, *9*(12), 3987–3997. <https://doi.org/10.5194/acp-9-3987-2009>

- Whitby, K. T. (1978). The physical characteristics of sulfur aerosols. *Atmospheric Environment*, *12*, 135–159. [https://doi.org/10.1016/0004-6981\(78\)90196-8](https://doi.org/10.1016/0004-6981(78)90196-8)
- Whitehead, J. D., Irwin, M., Allan, J. D., Good, N., & McFiggans, G. (2014). A meta-analysis of particle water uptake reconciliation studies. *Atmospheric Chemistry and Physics*, *14*(21), 11833–11841. <https://doi.org/10.5194/acp-14-11833-2014>
- Zíková, N., Pokorná, P., Makeš, O., Sedlák, P., Pešice, P., & Ždímal, V. (2020). Activation of atmospheric aerosols in fog and low clouds. *Atmospheric Environment*, *230*, 117490. <https://doi.org/10.1016/j.atmosenv.2020.117490>